



Caracterización e Identificación de Partículas Usando la Tecnología Skipper CCD

**(Characterization and Particle Identification
Using Skipper CCD Technology)**

**Trabajo de Fin de Máster
para acceder al**

MÁSTER EN FÍSICA DE PARTÍCULAS Y DEL COSMOS

Autor: Daniel Pérez Chamorro

Co-directora: Núria Castelló-Mor

Co-directora: Rocío Vilar Cortabitarte

Septiembre - 2024

Acknowledgements

Quisiera expresar mi más sincero agradecimiento a todo el personal del IFCA por el excelente trato recibido durante todo el curso. Un agradecimiento especial va para todo el profesorado del máster, cuyo apoyo y dedicación han sido fundamentales para el desarrollo de este trabajo.

Un agradecimiento particular a Rocío y a Nuria, quienes me enseñaron tanto y guiaron a lo largo del desarrollo del TFM. Ha sido un verdadero placer aprender tanto de ellas.

También deseo expresar mi gratitud a mis compañeros del máster. En especial, a Víctor y Antonio, por compartir tantas horas en la ya mítica esquina del IFCA, tanto en momentos de trabajo como de disfrute.

Asimismo, me gustaría agradecer particularmente a Sofía, por acompañarme siempre y estar ahí en los momentos buenos y malos.

Finalmente, quiero agradecer a mi familia por su incondicional apoyo en esta aventura. Su aliento y comprensión han sido cruciales para alcanzar este logro.

Abstract

Dark matter constitutes a significant portion of the Universe, yet our understanding of it remains limited. In this work, we focus on characterizing the IRONMAN experimental setup at IFCA, designed for dark matter direct detection utilizing Skipper-CCD technology capable of counting electrons. Despite the characterisation, we were unable to obtain quality images for scientific analysis. As an alternative, we used images from the MOSKITA detector at the LHC to develop a deep neural network capable of classifying the different types of particles detected. In addition, this neural network will be implemented in the official software of the DAMIC-M collaboration for future studies. Finally, using this neural network we verified that the number of muons is not directly correlated with luminosity.

Keywords: Dark matter, Skipper-CCD, MOSKITA, Hot columns, Deep Neural Network, Muon

Resumen

La materia oscura constituye una parte significativa del Universo, pero nuestra comprensión de la misma sigue siendo limitada. En este trabajo, nos centramos en la caracterización del montaje experimental del IFCA IRONMAN, diseñado para la detección directa de materia oscura y que utiliza tecnología Skipper-CCD capaz de contar electrones. A pesar de la caracterización, no pudimos obtener imágenes de calidad para el análisis científico. Como alternativa, utilizamos imágenes del detector MOSKITA en el LHC para desarrollar una red neuronal profunda capaz de clasificar los distintos tipos de partículas detectadas. Además, esta red neuronal se integrará en el software oficial de la colaboración DAMIC-M para futuros estudios. Finalmente, utilizando esta red neuronal, comprobamos que el número de muones no está directamente correlacionado con la luminosidad.

Palabras clave: Materia oscura, Skipper-CCD, MOSKITA, Columna caliente, Red Neuronal Profunda, Muon

Contents

Acknowledgements	I
Abstract	II
General Index	IV
Figure index	VI
Table index	VII
Motivation	VIII
1 Introduction	1
1.1 Dark Matter	1
1.1.1 Types of detection	2
1.2 Charge Coupled Devices	3
1.2.1 How do CCDs work?	3
1.3 Skipper-CCDs	7
1.4 DAMIC-M experiment	8
2 IRONMAN setup	12
2.1 Cryocooler	12
2.2 Vacuum pump	13
2.3 Detector chamber	13
2.4 Detector	13
2.5 LTA	14
2.6 Slow control	15
3 CCD characterization	16
3.1 CCD PP52	16
3.1.1 Vertical voltage optimization	19
3.1.2 Glowing study	19
3.2 Change of CCD and setup optimization	19
3.3 CCD PP13	21
3.3.1 DS9 Amplifiers distribution	22
3.3.2 Voltage gates optimization	22
3.3.3 Bias voltage	23

3.3.4	Unclocking serial register	24
3.3.5	Integration time	24
3.3.6	Skipper images	25
4	MOSKITA	27
4.1	Introduction	27
4.2	Data Cleaning	29
4.3	Hot Columns	34
4.4	Particle Classification	39
4.5	Number of Muons Per Day	44

Figure index

1.1	Different approaches for DM detection. Figure from [1]	2
1.2	Analogy of a CCD. Figure from [29]	4
1.3	Clocking diagram. Figure from [5]	5
1.4	Readout scheme. Figure from [5]	6
1.5	CDS technique. Figure from [5]	7
1.6	Gate diagram of the Skipper-CCD technology. Figure from [6]	7
1.7	Differences between the classical readout technique and the Skipper-CCD readout technology. Figure from [6]	8
1.8	Pixel readout noise vs the N_{skips} , fitted into a $\sigma_1/\sqrt{N_{skips}}$, where σ_1 is the readout noise for one skip. Figure from [11]	9
1.9	Single electron resolution achieved by the DAMIC-M collaboration using Skipper-CCD. Figure from [12]	11
1.10	DAMIC-M 90% C.L. upper limits (solid black) on DM-electron interactions through a ultra-light mediator (left) and heavy mediator (right). Figure from [13]	11
2.1	IRONMAN setup	12
2.2	Detector Chamber	14
2.3	CCD PP13	14
2.4	LTA used at the IRONMAN setup	15
3.1	CCD amplifier nomenclature	17
3.2	Image from the CCD PP52-U	18
3.3	Comparison of images with different exposition time, reading the L1 amplifier	20
3.4	CCD inner connection	21
3.5	First image using the PP13 splitting the charge into the four amplifiers	21
3.6	Amplifier distribution in the ds9 software	22
3.7	Particles with different V_{bias} to observe diffusion	24
3.8	Image taken with 1500 skips	26
4.1	MOSKITA setup and location	28
4.2	Pedestal Subtraction Process example	31
4.4	Dark current histogram for the amplifier 2	31
4.3	Fit Dark Current Process example	32
4.5	Dark current histogram for the amplifier 3	32
4.6	Gain histogram for the amplifier 2	33
4.7	Gain histogram for the amplifier 3	33

4.8	Image with three visible columns	34
4.9	Number of events with charge between $0e$ and $3e$ per column for amplifier number 2	35
4.10	Number of events with charge between 0 and $3e$ per column for amplifier number 3	35
4.11	Number of events with with charge between $0e$ and $3e$ per column with, the fit into a first order polynomial and the regions to determine if it is a hot column for the amplifier number 2	36
4.12	Number of events with charge between $0e$ and $3e$ per column, with the fit into a first order polynomial and the regions to determine if it is a hot column for the amplifier number 3	36
4.13	Apparent cold column	37
4.14	Number of events with any charge per column for the amplifier number 2	38
4.15	Density of events with charge between $0e$ and $3e$ vs the sigma for the amplifier 2	38
4.16	Saturation energy per pixel in the CCD per amplifier from the images taken the 15 of March 2024.	39
4.17	Different types of alphas.	40
4.18	Different types of electrons.	41
4.19	Muon.	41
4.20	Hot column.	42
4.21	Serial register event.	42
4.22	Multiple event of a muon and an electron.	43
4.23	Pixel density versus the energy of the cluster	43
4.24	Number of muons and luminosity versus the File number.	46

Table index

3.1	Optimal parameters from the last characterization. Values from [15].	17
3.2	Standard deviation comparison with the LTA cable and without.	19
3.3	Standard deviation comparison for the different VH.	19
3.4	Standard deviation of the different horizontal voltages.	23
3.5	Standard deviation of the different vertical voltages.	23
3.6	Standard deviation for the different PSAMP and SSAMP times.	25
3.7	Standard deviation for the different PINIT and SINIT times.	25
3.8	Optimal values for the parameters.	26
4.1	Dark current and gain for the different amplifiers using the images from the 15 of March 2024.	33

Motivation

Since the concept of dark matter was first proposed in the early twentieth century, many theories have emerged regarding its nature. These theories range from Primordial Black Holes formed shortly after the Big Bang, with masses several times that of the Sun, to Axions with masses on the order of 10^{-21} eV. Some theories even suggest that our understanding of gravity might be incomplete, leading to ideas such as Modified Newtonian Dynamics. Despite the increasing popularity of dark matter research, only a few properties of dark matter are known, and there is still much to be understood about its nature.

The motivation for this work arises from the desire to contribute to the detection and understanding of dark matter. This research is divided into two main parts. The first part focuses on hardware, where we will characterize the experimental setup used for the future characterization of other detectors in the DAMIC-M collaboration. The second part involves the development of software, aiming to develop a deep neural network capable of classifying particles detected by our detector and investigating whether the number of muons increases with the luminosity of the LHC.

The work is organized into four chapters. The first chapter introduces dark matter, its properties, the most popular candidates today, and the different approaches for its detection. We will also discuss the type of detector used, its operation, and the innovative Skipper readout technique, which allows for electron counting.

The second chapter provides a brief description of the various components of the IRONMAN setup we are working with.

In the third chapter, we will characterize the setup and the detector, focusing on the various tests conducted to optimize parameters.

The fourth and final chapter addresses the software aspect of the work. We will use images from the MOSKITA detector, located at the LHC, to train and test our deep neural network. Additionally, we will create a script to detect defects in the silicon detector, such as hot columns.

Chapter 1

Introduction

1.1 Dark Matter

As far as we know, our universe composition can be divided in three parts: First there is baryonic or standard matter, which includes visible elements such as radiation, atoms that make up the stars, planets or ourselves. This type of matter just constitutes around 5% of the Universe's composition.

The second component and the most abundant in the Universe, is dark energy which makes up around 68% of the Universe. Dark energy is thought to be responsible for the accelerated expansion of the Universe. Despite being the most abundant component, its nature remains unknown. Some hypothesis have been proposed regarding what it might be such as: quintessence, vacuum energy, or even an error in Einstein's general theory of relativity.

Finally, the third component and the focus of this work, is dark matter (DM). It accounts for around 27% of the Universe. DM has not been directly detected yet, and we only know some generic properties it should fulfill. It is termed "dark" because it does not emit or absorb electromagnetic radiation, making us impossible to detect it. In this work, we will review the current knowledge about DM, its main characteristics, its most popular candidates and the different approaches to detect it.

DM was first proposed in the twentieth century based on various observations at both astrophysical scales and large scales. At astrophysical scales, there are some gravitational effects that could be explained by the introduction of DM. For example, the rotation curves of galaxies, where the velocity of the stars, instead of decreasing with distance from the center of the galaxy, as Newtonian physics predicts, it remains constant. This observation is easily explained by introducing the presence of a DM halo surrounding the galaxies, which explains why stars far from the center have a constant velocity. In addition, galaxies need this DM to keep them from breaking apart and the stars from flying away.

At large scales, evidence for DM comes from cosmic microwave background calculations, the galaxy power spectrum and baryonic acoustic oscillations.

One way to know the distribution of the DM in the galaxies, is done by using gravitational lensing. From general relativity, we know that not only matter is affected by gravity but also light, so when light passes near an accumulation of mass, it bends. Then, if an object is behind an accumulation of the sufficient mass to bend the light, it can be observed multiple times. Because DM is massive and its accumulation in the galaxies can bend the light, galaxies behind one galaxy, can be observed multiple times. Depending on the distribution of the different galaxy images, DM can be mapped.

Although the existence of DM seems more plausible than other alternative theories such as modified gravity, its exact nature remains unknown. Various DM candidates have been proposed, and must fulfill several properties such as: being massive, neutral or milli-charged, stable or very long-lived of the order of the age of the Universe, non-relativistic or cold, interacting only gravitationally or very weakly, finally depending on the model, its mass can range from: $10^{-21} eV$ to several solar masses.

The most popular and studied DM candidates include: primordial black holes, axions or axion like particles, sterile neutrinos, hidden sectors, and the Weakly Interacting Massive Particles (WIMPs), which are particularly prominent in direct detection experiments.

Initially, WIMPs were the principal candidate for their search in Charge Coupled Devices (CCDs). However after several years of investigation, and new constraints on the mass range below the GeV, as well as an improvement in technology, new models emerged. Specifically, models from the hidden sector, which share some similar properties with classical WIMPs, but with the mass range on the order of MeVs have gained attention. In these models, DM can interact with electrons through inelastic scattering, producing an electronic recoil in the eV-scale. This interaction gives access to possible hidden-sector DM candidates that interact via a new gauge boson, which is feebly mixed with the photon. These are the primary models employed in the experiments conducted for this work.

1.1.1 Types of detection

There are three types of methods used for DM searches, there is an scheme in Figure 1.1.

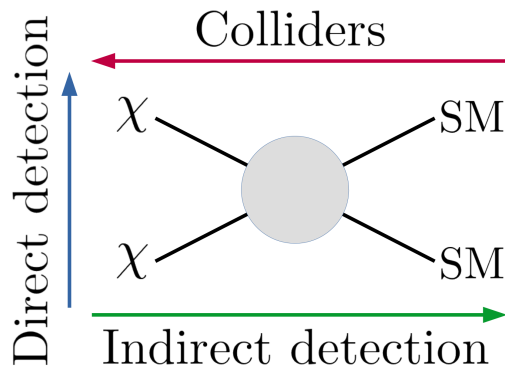


Figure 1.1: Different approaches for DM detection. Figure from [1]

The first method is indirect detection (ID), where we search for DM particles either colliding with each other and resulting in the creation of Standard Model (SM) particles or decaying into SM particles. Instruments used for ID include satellites, balloons and ground-based telescopes.

The second method is collider searches, where the aim is to produce DM after SM particles collide. In this type of searches, scientists are looking for missing energy transverse after a SM collision, which may indicate the presence of DM.

The third method is direct detection (DD), which involves looking for nuclei or electron recoil after DM interacts with our detector. The interaction between DM and SM particles can be observed through three different signals, depending on the technology of the detector used. These signals include: the production of heat (phonons in a crystal), an excitation of the target nucleus, which then de-excites by releasing scintillation photons or the direct ionization of the target atoms. The detection strategies typically involve one of these signals or a combination of two. While it is theoretically possible to study the three signals together, such an experiment have not been yet conducted.

In this work, we will focus on the DD approach, using CCDs, which are particularly sensitive to the electron recoil.

1.2 Charge Coupled Devices

Charge Coupled Devices (CCDs) were invented on October 19, 1969 by Willard S. Boyle and George E. Smith at Bell Telephone Laboratories. Originally conceived as memory devices, CCDs quickly demonstrated their potential as detectors. By the 1970s, Astronomers were the first to adopt CCDs for scientific purposes, replacing photographic film and revolutionizing the astronomy field.

1.2.1 How do CCDs work?

CCDs were originally designed as memory devices, serving as storage units for data and data movement instructions. The creation of CCDs involved the use the most cutting edge technologies of the time, including: magnetic bubbles, MOS semiconductor technology and the silicon diode array video camera tube (vidicon) for Picturephone.

The concept of magnetic bubbles in semiconductors is analogous to the storage of charge, where the presence or absence of charge, represents binary values (0 or 1). With this idea, we have a simple memory device. To store charge in a confined area, a simple MOS capacitor is employed. A series of MOS integrated circuits can store information, but the challenge remained moving the information (charge) around the device. This was solved by placing the MOS capacitors close together, allowing the charge to move by applying different voltages at lower or higher levels as required. The simplest method is to connect the MOS capacitors to a three-phase voltage source. This is how CCDs were developed.

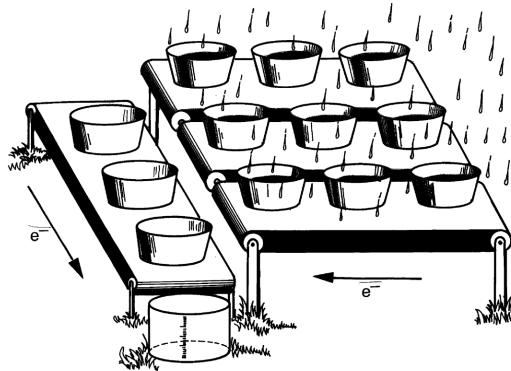


Figure 1.2: *Analogy of a CCD. Figure from [29].*

CCDs were originally conceived for computer memory, but soon they realized, in particular Michael F. Tompsett, also at Bell Labs, that with a small refinement the CCDs work better for imaging. Subsequently, Tompsett and other researchers continued to improve the CCDs, leading to improvements in light sensitivity and overall image quality. The CCD soon became the primary technology for digital imaging and was installed in cameras, phone cameras, and telescopes. Numerous telescopes, both in the space and on the ground, use CCDs: Hubble, ALMA, the Vera Rubin Observatory, the James Webb, the “Gran Telescopio de Canarias”, DESI, DES. The CCDs from the Dark Energy Survey (DES) have been used for the DAMIC experiments and have been upgraded to be more suitable for DM searches.

In our work, we are focused in using CCDs for DM search with direct methods. CCDs are essentially semiconductor devices. When a particle interacts with the silicon substrate of the CCD, it creates an electron/hole pair. Then, an electric field collects this charge into a potential well. Finally, the charge is moved through the CCD to an amplifier for readout.

In a CCD, diffusion of charge carriers works as follows: The CCD is a semiconductor in which holes are created within the bulk material. These holes are collected by applying a bias voltage, which generates an electric field that moves the holes at a drift velocity.

As the holes are displaced by the electric field, successive collisions with phonons and impurities in the lattice, impart a Brownian motion to them in a direction transverse to the electric field. This motion generates a net charge displacement from the region of higher concentration to the region of lower concentration, which is known as diffusion [4]. Local Coulomb forces also contribute to diffusion, the longer the holes remain in the bulk, the more significant the impact of these forces. Therefore, at greater depths, the Coulomb forces act for a longer duration, further enhancing the diffusion of the charge carriers. Consequently, the deeper the charges are within the bulk, the more significant the diffusion they experience compared to those nearer the surface.

The process of moving the charge through the different MOS capacitors in the detector is typically referred to as “clocking”. Each MOS capacitor or column/row is made up of three-phase voltage, where each phase is called a gate. The gates only have two states, high or low. This creates a voltage difference between the gates in such a way that the stored charge moves through the gates. Additionally, only one gate can change its state at a time. The process

of moving the charge through one MOS to another, can be done in seven steps. Figure 1.3, illustrates a schematic of these steps.

In Figure 1.3 it can be see the initial state (state 1), where gates 1 and 3 are set to high, while gate 2 is low. This configuration confines the charge generated by the interacting particle in the gate 2. To move the charge, gate 1 switches to the low state, causing the charge to split between gates 1 and 2. The next step involves changing gate 2 to the high state, transferring the charge into gate 1. By repeating these processes, the charge can go wherever we want.

The three gates operate with the same voltage values for their high and low states, and these parameters have must be finely tuned for the best performance of the CCDs. In addition to voltage, another parameter to be considered is the time gates remain in each position. This last parameter must also be tuned, if time is too short, charge may not transfer completely, leading to errors. On the other hand, if time is too long, the time required for each image will increase significantly. In addition, charge from another interaction can arrive at the gate in the low position.

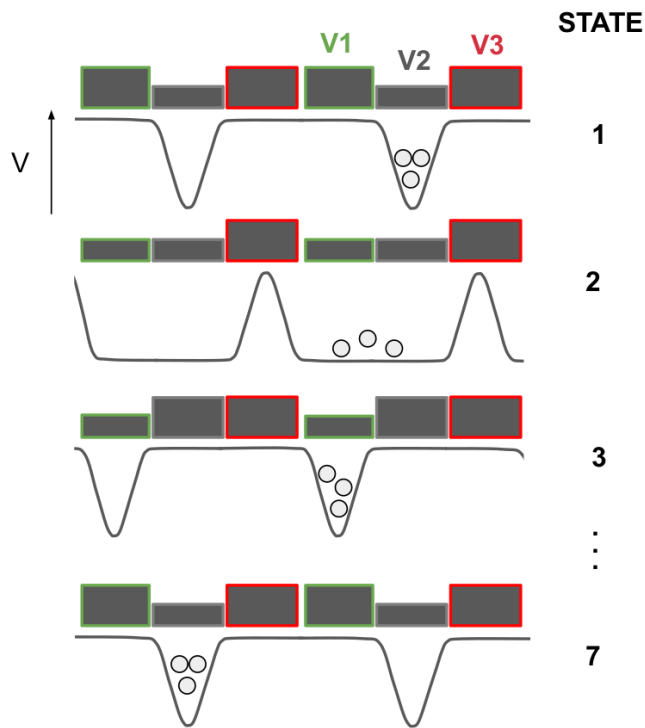


Figure 1.3: Clocking diagram. Figure from [5].

The CCD is a two dimensional detector that is read at the horizontal ends of the first row, where the amplifiers are located. This means that the charge must first move through the columns and then through the rows. The clocks that move the charge across the columns are called horizontal clocks. The clocks that move the charge through the rows are called vertical clocks.

The first row is called the “serial register”. The aim is to move all the charge into the serial register for reading. To achieve this, the charge from the CCD rows is first transferred downwards so that a whole row reaches the serial register. Then each charge in the serial register is moved horizontally to the amplifier. This process is repeated for all CCD rows. It is important to note that the horizontal clocks must be faster than the vertical clocks, as each complete row must be read horizontally into the serial register before the next row.

To regulate when charge can enter the serial register, there is the “transfer gate” (TG). It creates a potential barrier, and only when it is open, charge can enter the serial register.

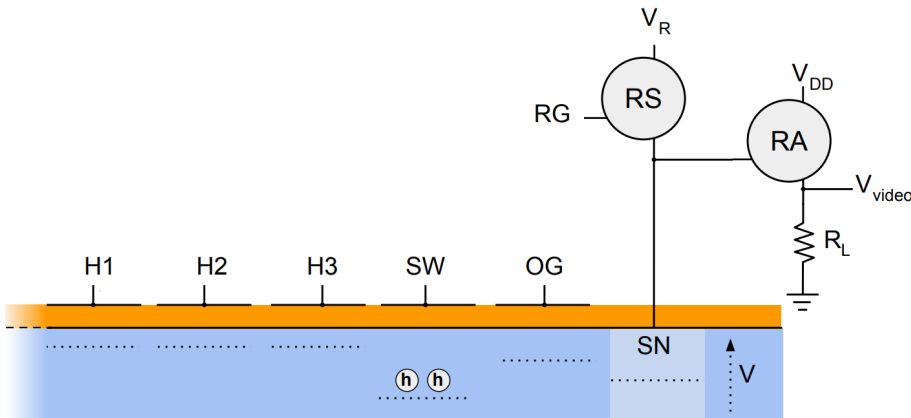


Figure 1.4: Readout scheme. Figure from [5].

Before the charged is completely readout and send away, it passes through a series of gates, in Figure 1.4 there is a scheme of the different gates. First, the charge enters the “summing well” (SW), where the charge from one or multiple pixels can be collected. In this step, it is possible to increase the signal-to-noise ratio or to measure the total charge accumulated in the serial register. The next gate is the “output gate” (OG), which controls the flow of charge between the SW and the “sense node” (SN). The SN gate measures the pixel charge and consists of a capacitor set to a reference bias voltage V_R .

Prior to reading the next row, the charge in the SN must be drained, this is accomplished via a reset pulse. However, this reset pulse injects fake charge values, which manifest as noise. In order to address this issue, the Correlated Double Sampling (CDS) technique is used, which consists on measuring the charge at the SN twice. The first measurement is taken after the reset pulse, when the charge has not yet entered the SN. During this period, the charge present in the SN is measured during an integration time τ_{int1} , providing the pedestal value. The second measurement is taken once the charge has entered the SN, it is also measured over a different integration time τ_{int2} , which corresponds to the signal value. The CDS technique is depicted in Figure 1.5, where the reset pulses, the integration times and possible different charge levels are shown. By subtracting the pedestal value to the signal, noise is suppressed. Upon applying the CDS technique, only high-frequency noise is significantly reduced, while low-frequency noise remains unaffected.

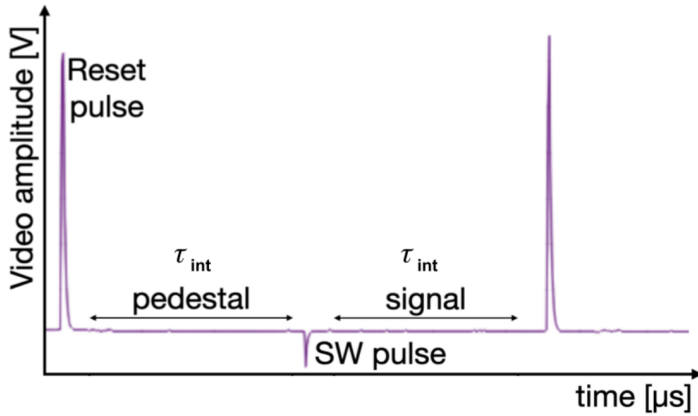


Figure 1.5: CDS technique. Figure from [5].

1.3 Skipper-CCDs

In the previous section, we reviewed the classical or typical readout for CCDs, which is the most widely used technique in astronomy. However, this is not the only technique used in the DM experiments.

As we have seen, noise is introduced whenever we drain the charge, although the CDS technique reduces high frequency noise to a point of almost elimination, it does not reduce low-frequency noise.

In order to solve this limitation, Janesick *et al.* [7] proposed a method to reduce low-frequency noise by using a floating gate as the SN, and performing repeated non-destructive measurements of the charge in each pixel. The repeated measurements are referred to as “skips”, then, the technique is called “Skipper”. In the skipper technology, once the charge is at the SN, instead of draining it, the floating gate, reduces its voltage so that the charge can be moved to the SW, and then again to the SN for a new measurement. Figure 1.6 depicts the Skipper-CCD technique. The number of skips can be adjusted to achieve the desired resolution. To drain the charge, we have to introduce an additional gate called “Dump Gate” (DG).

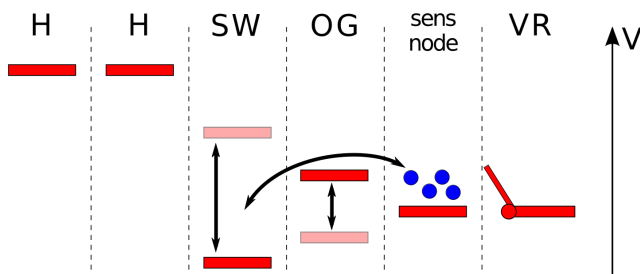


Figure 1.6: Gate diagram of the Skipper-CCD technology. Figure from [6].

The measurement is non-destructive because the charge is not drained until the completely

readout of all the skips, and each skip performs an independent measurement. The final pixel value is calculated as the mean of all the measurements. In this way, the low-frequency noise compensates and is eliminated.

In Figure 1.7 there is a comparison between the CDS technique and the skipper technology. In both cases, the high frequency noise compensates because in the time it takes to take a measurement, the high frequency noise has different high and low values, so the sum of them compensates. Meanwhile, in the time it takes to take a measurement with the CDS technique, the low frequency noise has a large difference between the high and low values. With the Skipper technique, however, there are more and faster measurements, which leads to a compensation between the different high and low noise values. Also, the average of the different measurements eventually eliminates this low frequency noise.

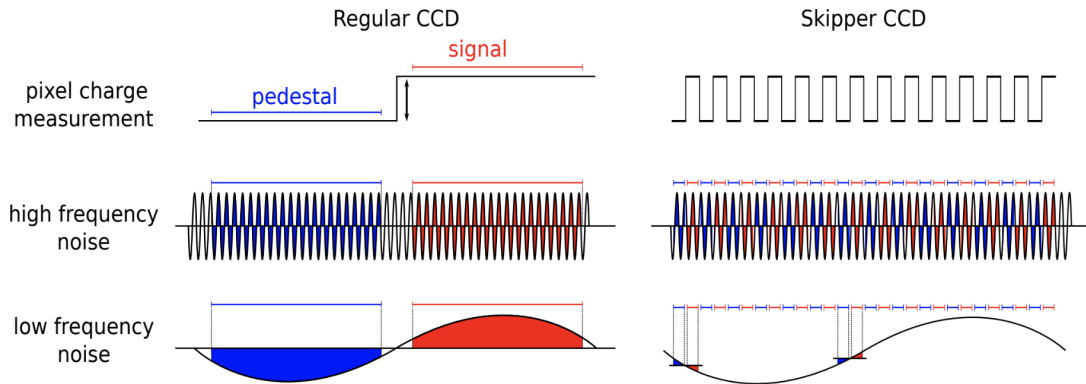


Figure 1.7: Differences between the classical readout technique and the Skipper-CCD readout technology. Figure from [6].

The pixel readout noise decays with the square root of the number of skips $\sqrt{N_{\text{skips}}}$, as shown in Figure 1.8. In this figure, the number of skips is represented vs the pixel readout noise, it can be observed that the more skips the less noise. However, it has to be considered that the total time to readout the CCD increases and this could lead to other backgrounds such as the dark current. Dark current is a current that arises mainly from thermal generation but also from charge injection, recombination, tunneling and leakage current [28]. Therefore, the more skips we do, the less noise we have, but the time for the whole measurement increases. So we have to choose a sufficient number of skips to reduce the noise to the desired level.

1.4 DAMIC experiment

The DArk Matter In CCDs (DAMIC) experiment originated at the Fermi National Accelerator Laboratory (Fermilab), where it was assembled using surplus Charge-Coupled Devices (CCDs) from the Dark Energy Survey (DES) experiment. These scientific CCDs, known for their high resolution and low noise, were adapted for dark matter (DM) detection. To minimize the impact of radioactive backgrounds, the DAMIC collaboration installed a shield around the

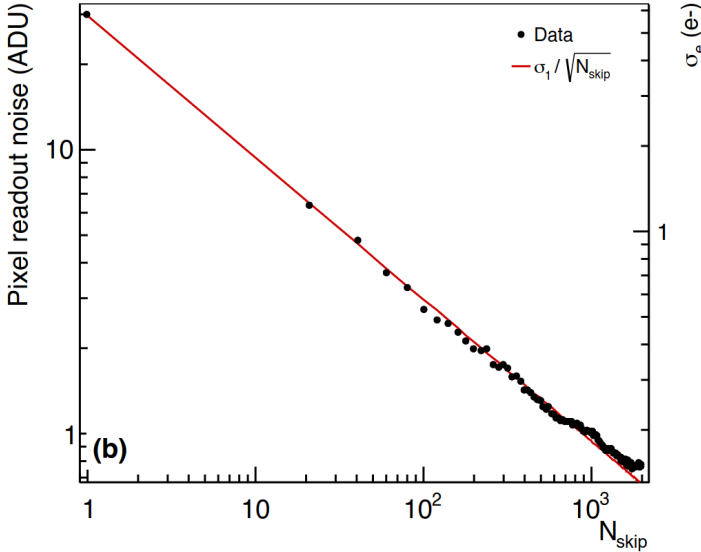


Figure 1.8: Pixel readout noise vs the N_{skip} , fitted into a $\sigma_1 / \sqrt{N_{\text{skip}}}$, where σ_1 is the readout noise for one skip. Figure from [11].

detectors. The experiment was conducted at the SNOLAB underground laboratory in Canada, this phase of the experiment was known as DAMIC-SNOLAB.

DAMIC-SNOLAB has been operating since 2016, providing significant results. However, to improve sensitivity for dark matter detection, further reduction of background rates and an increase in the active detector mass were required. In response, in 2018, a new collaboration called DAMIC-M (DArk Matter in CCDs at Modane) was formed. This new phase aims to install a more advanced experiment at the Laboratoire Souterrain de Modane (LSM) in the French Alps. DAMIC-M will use larger CCDs with lower background rates, and incorporate improvements in electronics such as the skipper technology, as well as enhancements in detector design.

The DAMIC-M experiment searches for sub-GeV dark matter. The thick silicon bulk of the CCDs allows for the detection of dark matter-induced ionization events with sub-electron resolution through non-destructive, repeated pixel readout. Combined with an extremely low dark current, this sensitivity enables DAMIC-M to achieve an energy threshold of a few eV. The completed experiment will feature approximately 700 g of target mass with an expected total background of a fraction of a dru (evt/kg/day/kev, differential rate unit). A prototype detector, the Low Background Chamber (LBC), is currently operating at LSM to demonstrate the performance of the CCDs, background control strategy, and sensitivity to light dark matter.

Currently, DAMIC-M is in the installation phase. The collaboration has made significant progress, such as producing silicon wafers with low cosmogenic activation and minimal radon contamination by limiting the time materials spend above ground during fabrication, transport, and storage. Low-background packaging techniques have also been implemented to ensure that the CCDs are surrounded by clean materials.

A prototype module consisting of four CCDs was successfully assembled at the University of Washington. Additionally, a total array of 200-CCD has been designed, consisting of 50 modules, each with 4 CCDs. This array will be housed in an electroformed copper cryostat, featuring protection with layers of ancient lead and an external shield of lead and polyethylene. Several campaigns have been conducted to characterize the detector's performance and background reduction capabilities. Recent advancements include measuring Compton scattering on silicon down to thresholds of 23 eV, and ongoing efforts focus on ionization efficiencies for nuclear recoils at even lower thresholds.

The DAMIC-M collaboration [11] has been working for several years with the skipper-CCD technology. With $N_{\text{skips}} = 2000$, the noise level has been reduced to $\sigma_e = 0.13e^-$. The sub-electron noise leads to a high resolution, that allows to be sensitive to energies as small as $2 - 3eV$. Also, single electron resolution is achieved, it is possible to count electrons, as we can see in Figure 1.9.

The exceptional resolution of the CCDs has been validated across various institutions, confirming their ability to detect single electrons. The Low Background Chamber (LBC), a prototype detector, has been installed at LSM, facilitating the collaboration's experience in operating underground detectors and managing low-background materials. Initial results from the LBC's dark matter-electron scattering search are now available.

The DAMIC-M experiment has established significant new constraints on DM particles. As depicted in Figure 1.10, the search has excluded regions of the parameter space for DM particles ranging from 0.53 to $1000 \text{ MeV}/c^2$, excluding regions of the parameter space in the mass ranges of $[1.6, 1000] \text{ MeV}/c^2$ for an ultra-light mediator and between 1.5 and $15.1 \text{ MeV}/c^2$ for a heavy mediator.

DAMIC-M continues to progress, including improvements in the fabrication of low-background components, such as flexible cables developed with PNNL, advancements in electronics for CCD controllers, and ongoing evaluation of DAMIC-M prototype performance.

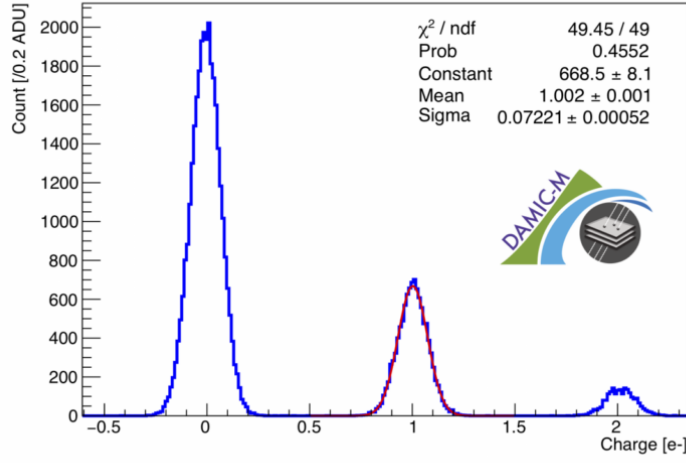


Figure 1.9: Single electron resolution achieved by the DAMIC-M collaboration using Skipper-CCD. Figure from [12].

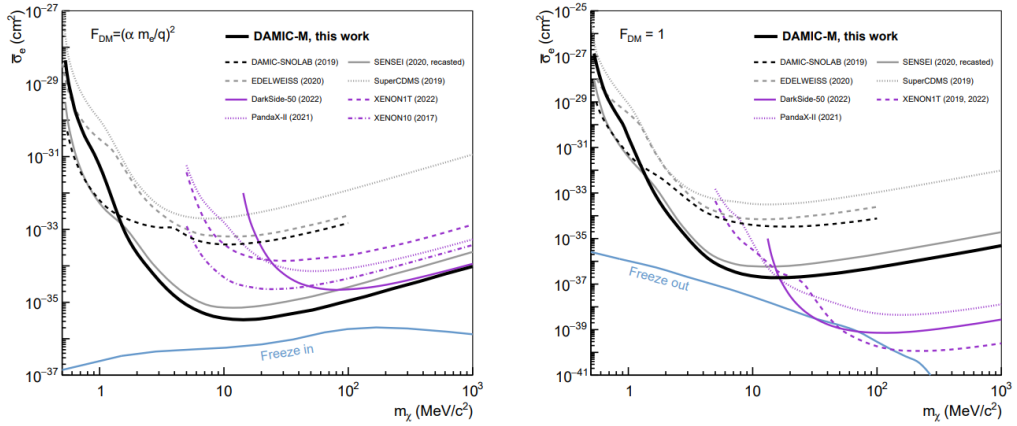


Figure 1.10: DAMIC-M 90% C.L. upper limits (solid black) on DM-electron interactions through a ultra-light mediator (left) and heavy mediator (right). Figure from [13].

Chapter 2

IRONMAN setup

In the “Instituto de Física de Cantabria” (IFCA) clean room, it is located an experimental setup, Figure 2.1, named IRONMAN, for the direct detection of dark matter. We are using a skipper-CCD that was used to test the DAMIC-M CCDs. The objective in this part of the work is to obtain the optimal values for the main parameters of the readout of the CCD, as explained in the previous chapter, the horizontal, vertical voltages and the voltages for the readout gates. Once we have obtained the best parameters, we will be able to do different studies that will be used for the DAMIC-M, OSCURA experiments and MOSKITA. During this chapter, we are going to explore the different parts that make up the setup.



Figure 2.1: Image of the setup with the different parts that compose it.

2.1 Cryocooler

The cryocooler is responsible for allowing us to reduce the temperature to those used at LBC/DAMIC-M, 130-120K, to reduce the dark current. The rate of the temperature reduction

is $0.015K/s$, this rate is recommended by scientists who work on the DAMIC-M and OSCURA experiments to prevent stress on the silicon of the CCD and the electronics caused by rapid temperature changes.

2.2 Vacuum pump

With the vacuum pump, we can reduce the pressure to the order of $10^{-8}mbar$. The main purpose of having a vacuum, is to prevent condensation when lowering the temperature, as condensation can damage the channels. Another advantage of reducing the pressure is that the concentration of Radon 222 or any other impurity present inside the chamber is reduced. Radon 222 emits alpha and beta particles when it decays [31].

2.3 Detector chamber

The detector chamber is a stainless steel structure that isolates the CCD both physically and electromagnetically from the environment, which is crucial for reducing measurement noise. This isolation protects the CCD from vibrations, electromagnetic interference and other external factors that could affect its sensitivity. In addition, the chamber maintains a controlled low-temperature and vacuum environment, minimising thermal noise. As shown in Figure 2.2, the CCD is placed inside the chamber, connected to the cryocooler at the top, and to the readout system at the bottom through the golden flexible flat cable (flex cable). Flex cables are used for their flexibility, durability in low-temperature environments, and suitability for compact spaces.

2.4 Detector

As a detector, we are going to use two non-scientific CCD labeled PP13 and PP52, with identical number of columns and rows, 6144×1536 . Every pixel has an area of $15\mu m \times 15\mu m$, corresponding to physical dimensions of $9.22cm \times 2.3cm$. CCD is depicted in Figure 2.3, It has four amplifiers for charge readout, located in the corners of the CCD. These amplifiers are connected to the flex cables through the darker lines.

The CCDs were made by the Canadian manufacturer DALSA. Then, the flex cables were soldered to the CCDs and placed in the box at the University of Chicago and finally shipped to IFCA.

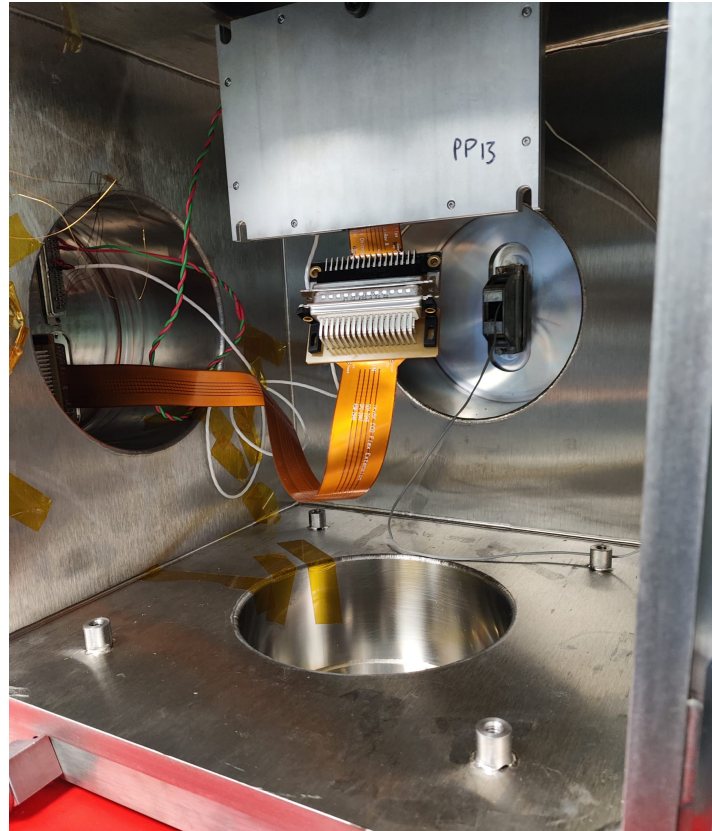


Figure 2.2: *Detector Chamber.*

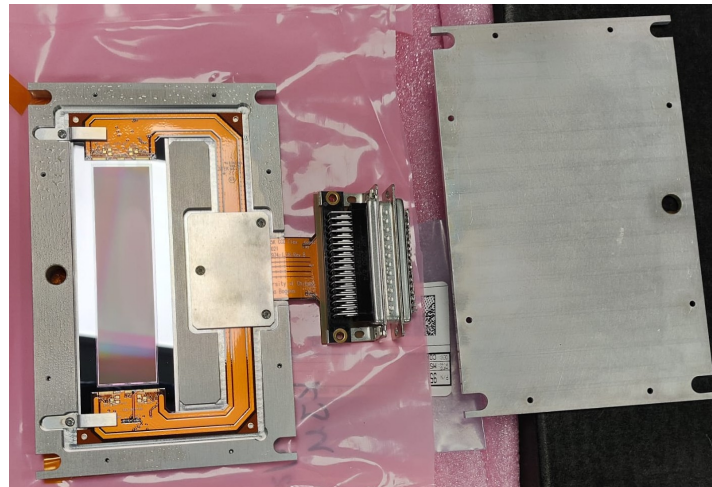


Figure 2.3: *CCD PP13.*

2.5 LTA

The main innovation in this set-up, compared to the previous one, was to update the data acquisition hardware from the LEACH system -a very old commercial system adapted to the specific requirements- to the new Low Threshold Acquisition (LTA) [14] controller, depicted in

Figure 2.4.

Measurements with the LEACH were limited by the noise induced during the readout electronics. To address this issue, the LTA was specifically designed to read skipper CCDs. The main advantages of the LTA include its compact design and superior noise performance. It has already proven to be the necessary solution in several experiments, such as SENSEI DAMIC which used skipper-CCD technology for the direct detection of DM.



Figure 2.4: LTA used at the IRONMAN setup.

2.6 Slow control

The Slow Control (SC) system is a critical component for remotely operating and monitoring key parameters in a CCD experimental setup. The SC system allows users to control instruments and adjust parameters such as power output, voltages, and temperature settings via a PHP-based web interface. The system, developed in collaboration with the DAMIC-M group at the University of Chicago, uses a C backend and MySQL for database management. It supports real-time monitoring, graphical data visualization, and alarm notifications when parameters exceed set thresholds, ensuring the system's safety and reliability. Communication with instruments is primarily through Ethernet.

Note that it is important to connect the LTA to the computer directly through Ethernet, with no intermediate adapters, to avoid possible disconnections or loss of data making it impossible to take images.

Chapter 3

CCD characterization

In this chapter, we will be looking for the optimal parameters for the detector readout. As we said in the previous chapter, there has been a significant upgrade in the IRONMAN setup, the change on the data acquisition hardware from the LEACH to the LTA. A priori, the images taken with the LTA will have less noise. The main objective, is to establish an optimal lecture setup for Skipper-CCDs, with the aim of having a setup where other scientific Skipper-CCDs can be characterised and used in different experiments, i.e. radio purity at the Laboratorio Subterraneo de Canfranc (LSC).

We will be working the PP13-U and PP52-U CCDs, that are not scientific. Last year, the PP52 was characterised with the LEACH data acquisition system [15]. Now, it is our turn to fully understand the LTA and create a space to characterise scientific CCDs substituting the LEACH.

The CCDs are equipped with four amplifiers, one at each corner, as shown in Figure 2.3. This configuration allow us to send the charge to the amplifier of our choice or to split the charge between two or four amplifiers to reduce the readout time. This choice can be done by modifying the sequencer file, in 4.5. Each of the four amplifiers on the CCD has a specific name, with the nomenclature divided into left/right and top/bottom directions, as shown in Figure 3.1. The left side of the CCD is labeled “L” and the right side “U”. The top part is identified as “1” and the bottom part as “2”. We will refer to each amplifier using the letter (L, U) followed by the number (1, 2). For example, Amplifier U1.

3.1 CCD PP52

We will start working with the PP52 CCD, the one used from the last characterisation. From it, we know that the only working amplifiers were the two on serial register 1, the top one in our scheme. To check that both amplifiers are still working correctly, we will take two images, first sending the charge to amplifier L1 and then to amplifier U1. After doing this,



Figure 3.1: *CCD amplifier nomenclature.*

we only observe particle traces in amplifier L1, suggesting that amplifier U1 may have stopped working. Note that this amplifier, U1, gave better results in terms of noise during the last characterisation, so we will now have to work with a worse one.

As a first contact, we will take an image with the optimal parameters from the last characterisation [15], the parameters are in Table 3.1, and the resulting image is presented in Figure 3.2. In this image, we can see some particle traces such as muons, betas and others. But also, we can see that there is glowing coming from the left part, affecting approximately 25% of the CCD, also we can appreciate a defect in the upper right side of it. These defects were not present in the previous characterisation, perhaps during the period of inactivity, apart from the U1 amplifier being damaged, the CCD or the amplifier has suffered some kind of damage, such an electric peak since the LEACH was also damaged.

Parameter	Low Value (V)	High Value (V)	Time (μs)	Voltage (V)
Vertical gates	4.5	1.5	30	
Horizontal gates	2	-0.5	1.25	
Transfer Gate	4	1.5		
Summing Well	-3	-10	-0.24	
Output Gate	-4	-9	0.24	
Dump Gate	-4	-8	0.24	
Reset Gate	5	3	0.24	
PINIT, SINIT			2.5	
Bias Voltage				60

Table 3.1: *Optimal parameters from the last characterization. Values from [15].*

If we examine the rest of the image, excluding the glowing effect, we can observe a kind of

“waves”. This pattern is likely caused by correlated noise, which could be due to electromagnetic interference. Possible sources of this interference include inadequate grounding, issues with the electronics of the setup, or external factors, because in the IFCA’s clean room, apart from the IRONMAN set up, there are other set ups that can induce electromagnetic noise when in operation.

Another issue is that the charge level of the pixels in the CCD is very high. This means the background signal, or pedestal, is also high, which can hide the particle traces we want to see. As a result, it becomes difficult to detect and analyze these traces accurately because the high background can overshadow the signals from the particles.

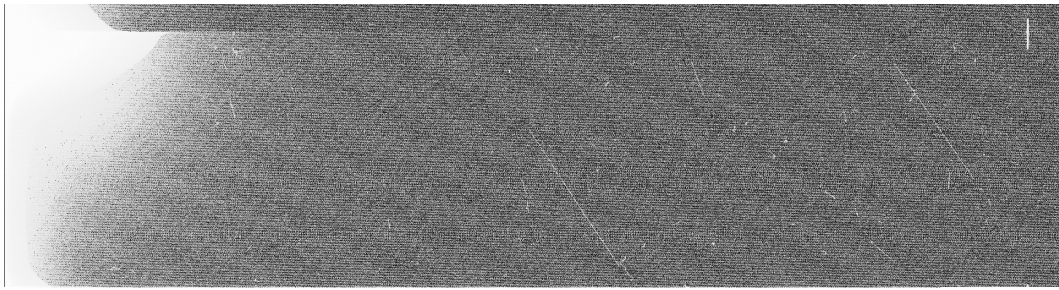


Figure 3.2: Image from the CCD PP52-U.

The ideal way to analyze the quality of the images is to use the official software of the DAMIC-M collaboration, WADERs. This software provides various tools for reading and processing the images. For more details, see the WADERs documentation [30]. Unfortunately, both the glowing and electromagnetic noise were so high that the various processes performed by WADERs, were not useful. Therefore, in order to do a very preliminary study, the DS9 software was used, the same one we use to visualise the images. The software performs a Gaussian statistical analysis of the region drawn over the images with the mouse. The sigma of this Gaussian is used by us to determine the quality of the parameters tested.

The background noise, at first orders, can be modeled as Gaussian. A high standard deviation indicates the presence of correlated noise or that the modified parameter may not be the optimal, while a low standard deviation suggests minimal electromagnetic noise or a good modified parameter. To carry out the tests most effectively, we need to ensure the following:

- No particles should be present when selecting the region.
- The selected area must be consistent in size and position across different images.
- The exposure time must be the same for all images to ensure uniform dark current.

One of the first steps we will do, is to try to reduce the electromagnetic noise as much as possible. So in order to reduce this noise, we will revised the grounding of the setup by probing different configurations of groundings. after several tries, the best configuration was connecting the LTA and the vacuum to the chamber and left the cryo floating. The results, presented in Table 3.2, demonstrate that this cable significantly reduces electromagnetic noise. This was tested several times and in all of them we observed this reduction. Therefore, this cable will remain part of the setup for the rest of the characterisation.

Standard deviation	
No cable	Cable
41000	36000

Table 3.2: Standard deviation comparison with the LTA cable and without.

3.1.1 Vertical voltage optimization

After reducing electromagnetic noise with the cable solution, our next step will be find the optimal voltage for the vertical gates when in the up position, referred to as voltage high (VH). The voltage in the down position, voltage low (VL), will remain fixed at 1.5V, while VH will be varied from 3V to 5.5V. The standard deviation values obtained at different voltages are presented in Table 3.3. It is clear that when the difference between VH and VL is smaller, the charge moves less efficiently, which can result in incomplete charge transfer when the gate switches to the up position, leaving some charge not transferred. The optimal voltage appears to be between 4V and 4.5V. We will choose VH = 4.5V, which is consistent with the optimal voltage from the previous characterization, as seen in Table 3.1.

VH (V)	3	3.5	4	4.5	5	5.5
Std. dev.	47000	44000	37000	36000	39000	41000

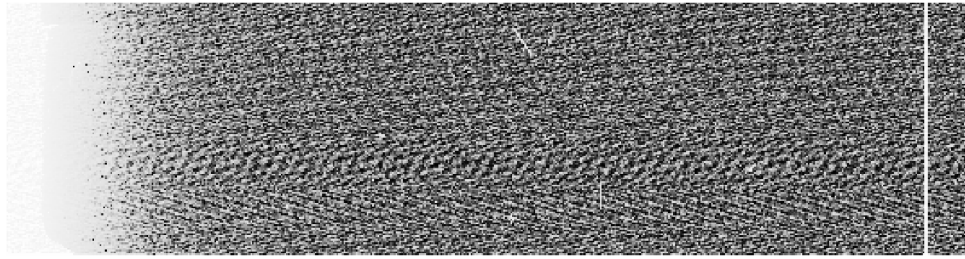
Table 3.3: Standard deviation comparison for the different VH.

3.1.2 Glowing study

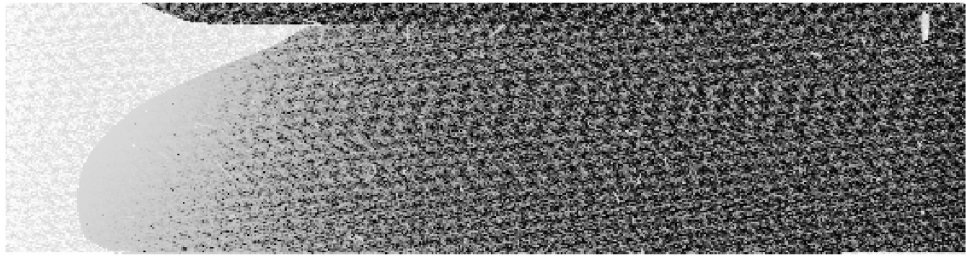
In all the images we took to optimize the vertical voltage, we observed that while the correlated noise decreased, the glowing persisted. Therefore, instead of continuing to search for the optimal values for other parameters, we will focus on eliminating this persistent glowing. To investigate its possible origin, we will first take one image without exposure time, as shown in Figure 3.3(a) and another one with two minutes of exposure time, in Figure 3.3(b). It is clearly evident that the glowing is proportional to the exposure time, as if something is injecting charges into the CCD. We also attempted unclocking the serial register 2, meaning that the gates from the readout of serial register 2 (see Figure 1.4) remain stationary and cannot inject any charges. However, the glowing still appears. Due to a lack of time, we were unable to unlock the U. Our final hypothesis, is that the glowing is induced by something inside the CCD chamber.

3.2 Change of CCD and setup optimization

With the hypothesis about the origin of the glowing issue, we can now proceed with the following actions. We will open the camera and replace the CCD with a PP13-U model, as the PP52 has been used extensively and currently has only one functional amplifier. Additionally,



(a) Image of zero exposition time.



(b) Image of two minutes exposition time.

Figure 3.3: Comparison of images with different exposition time, reading the L1 amplifier.

we will organize all the cables, remove any unnecessary devices from the setup, and connect the electronics' power supply to an uninterruptible power supply (UPS).

To open the chamber, we first required a few hours to stabilize the pressure and temperature. Once the chamber conditions were set, we proceeded to open it, remove the PP52 CCD, and prepare for the installation of the PP13-U. Before connecting the new CCD, we will verify that it is electromagnetically isolated. Using a multimeter, one probe will contact various parts of the chamber while the other probe will contact the CCD. We have found that everything is isolated except for the "L" copper bar, which mounts the CCD and connects it to the cryocooler, as illustrated in Figure 3.4.

The issue arises from a wire protruding from the temperature sensor, which makes contact with the "L" bar, compromising the CCD's electromagnetic isolation. To address this, we will apply thermal paste to the L bar. This thermal paste, while an excellent conductor of heat, also acts as an electromagnetic insulator, allowing the cryocooler to effectively cool the CCD while ensuring proper isolation. Before and after connecting the CCD and closing the chamber, we will recheck the CCD's electromagnetic isolation to ensure it is adequately insulated.

The next step involves removing any unnecessary electronics from the setup, which is a straightforward task. Following this, we will enhance the grounding to minimize electromagnetic noise. We will begin by disconnecting all electronic devices, connecting them to a single power strip, and linking this strip to an uninterruptible power supply (UPS) for improved stability. This ensures that all electronic devices receive the same frequency and voltage from the power supply.

To further improve grounding, we will cover the cables connecting the chamber to the amplifiers, LTA, cryocooler, and vacuum pump with Kapton flex if they are in contact with other cables. Kapton flex provides electrical insulation for the cables. Additionally, all equipment and electronics will be connected to ground to ensure proper grounding.

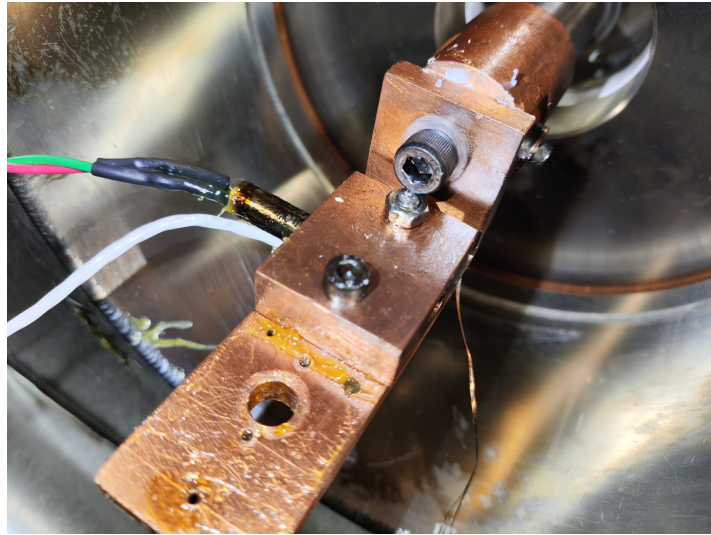


Figure 3.4: Connection between the set point heater of the cryocooler and the CCD, also with the sensor to measure the temperature.

3.3 CCD PP13

After all the changes done in the setup, we are ready to start the characterization of the setup with the CCD PP13. The experimental pressure and temperature conditions for this characterization are as follows: the temperature will be set to 130K, and the pressure will be maintained at approximately $8 \cdot 10^{-8}$ mbar.

Since this CCD hasn't been used in a while, we are not sure which amplifiers are working. To figure this out, we will split the charge among the four amplifiers and take an image, shown in Figure 3.5. The image clearly shows that only three amplifiers are working. Additionally, the pixel value has dropped by two orders of magnitude, which will make particle traces more distinct and easier to identify, also we will have a better clustering. Thanks to better grounding and a cleaner workspace, the correlated noise appears to have disappeared. Also the standard

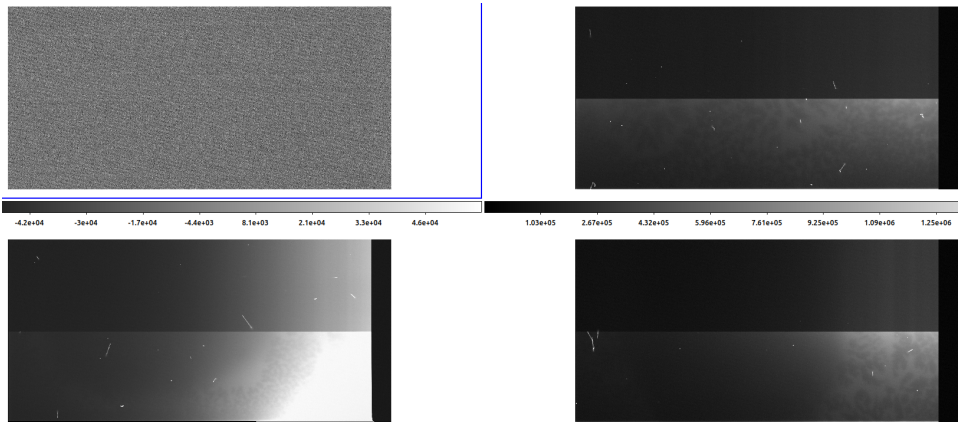


Figure 3.5: First image using the PP13 splitting the charge into the four amplifiers.

deviation has been reduced around one order of magnitude just with these changes.

3.3.1 DS9 Amplifiers distribution

The next couples of images are going to be taken in order to know what are the working amplifiers in the nomenclature we use, Figure 3.1, and to know how the amplifiers are distributed in the DS9 software. There is a substantial difference between the previous readout system (LEACH) and the new one (LTA). With the LEACH, we only get a single image for the amplifier(s) we are reading. However, in the LTA, we get one image for each amplifier whether it is being read or not. Note that this image always places the amplifier as if it is in the bottom-left corner, therefore, we have to do a translation of the images. This means that we do not know how the amplifiers are distributed. We are going to take four images where we will send the charge to the four different amplifiers.

The scheme distribution of the amplifiers is depicted in Figure 3.6. The serial register 1, is the left column of DS9, meanwhile the serial register 2 is the right column. The top row is the L part, and the bottom row is the U side. This is important for us to know the distribution of the charge and to know where the glowing comes from. The only amplifier that is not working is the top left one, the L1.

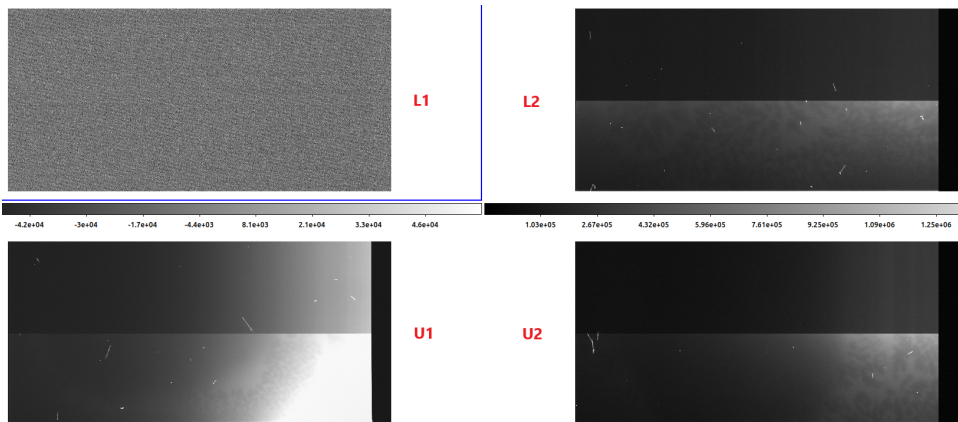


Figure 3.6: Amplifier distribution in the ds9 software.

3.3.2 Voltage gates optimization

Now, we are going to obtain the optimal VH and the equivalent for the horizontal gates, HH. We will read the charges collected for the four amplifiers simultaneously. If the voltage difference between the high and low states is too small, the charge movement may be ineffective, resulting in an image with vertical or horizontal stripes, making the image appear striped.

Horizontal voltage gates

We will start by changing the voltages of the horizontal gates, we will start with an $\text{HH} = 1V$, and we will increase the voltage $0.5V$ per image and again, the HL will remain constant with a value of $\text{HL} = -0.5V$. The results are presented in Table 3.4, we can see that the

HH (V)	2	2.5	3	3.5	4
Std. dev.	3180	3170	3180	3180	3240

Table 3.4: Standard deviation of the different horizontal voltages.

optimal HH voltage is $2.5V$ which is slightly better than the other voltages.

Vertical voltage gates

For the voltages of the vertical gates, we will start from $\text{VH} = 3.5V$, increasing $0.5V$ per image till $5.5V$, meanwhile the VL will not change, remaining constant with a value of $\text{VL} = -1V$. The results are presented in Table 3.5, the optimal VH is $4.5V$.

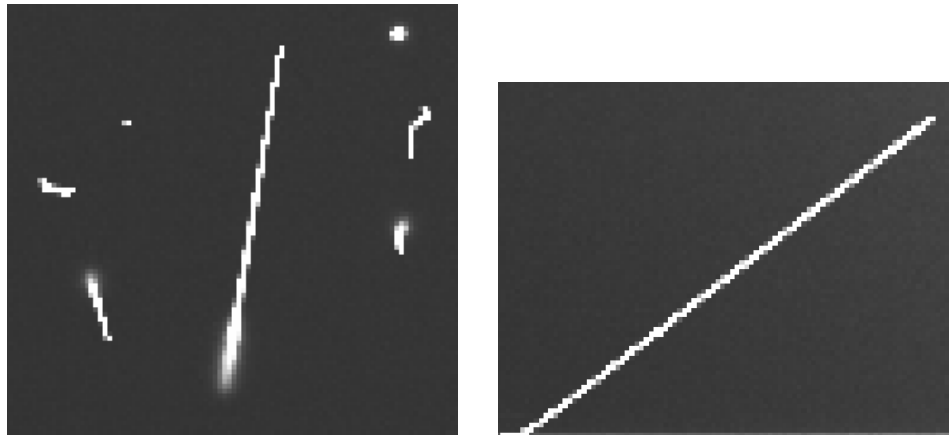
VH (V)	3.5	4	4.5	5	5.5
Std. dev.	3130	3120	3080	3130	3110

Table 3.5: Standard deviation of the different vertical voltages.

These values for VH and HH are in consistency with the results from the previous characterization [15].

3.3.3 Bias voltage

Since the CCD is a semiconductor, in order to collect the charges created after the CCD's exposition, we need an electric field. This electric field is created by applying a bias voltage (V_{bias}) across the device. A higher V_{bias} results in a stronger electric field, which implies faster charge collection and, consequently, reducing diffusion. We will search for the optimal V_{bias} , starting from $30V$, having into account that the maximum voltage is $70V$. With a low V_{bias} , we observe diffusion in the tails of the particles, as shown in Figure 3.7(a), but with less noise, as indicated by the standard deviation. If the V_{bias} is high, we will not have diffusion, as seen in Figure 3.7 but we will more noise according to the standard deviation. Then, we need to find a balance between minimizing diffusion and reducing the standard deviation. While diffusion is essential for accurate 3D reconstruction and determining the depth of interactions, it also contributes to background noise. Therefore, optimizing this balance helps in reducing surface or background noise while maintaining the ability to reconstruct interactions in three dimensions. The first bias voltage at which particles have no diffusion, is observed at $V_{bias} = 40V$. To allow a margin of error, the optimal V_{bias} can be either $45V$ or $50V$.



(a) Particle with diffusion, $V_{bias} = 30V$. (b) Particle without diffusion, $V_{bias} = 40V$.

Figure 3.7: Particles with different V_{bias} to observe diffusion.

3.3.4 Unclocking serial register

Despite the modifications made to the setup and the optimization of several parameters, we continue to experience glowing but in a minor way compared to the PP52 images, and only in one amplifier (L2). The same as we did with the other CCD, we are going to unlock the serial register 2 and send all the charge to the L1 amplifier. The glowing now is on the amplifier L1, we can try to unlock the serial register 1, but still the glowing appears.

Our hypothesis is that the issue with the L cooper bar has not been fully resolved. It is possible that during the CCD cooldown and pressure reduction, the positioning of this component might have shifted. This misalignment could lead to the induction of unwanted charge. Specifically, we suspect that inadequate insulation between the L cooper bar and the cryocooler head might have contributed to this issue.

3.3.5 Integration time

The last parameters we are going to change are the ones related to the CDS readout technique, as depicted in Figure 1.5. There are four parameters that can be optimized: PSAMP, SSAMP, PINIT and SINIT. PSAMP is the measurement time for the pedestal, while SSAMP is the measurement time for the signal. PINIT is the waiting time before the reset pulse and after the pedestal measurement, and SINIT is the waiting time after the reset pulse and before the signal measurement. We will set the same time for PSAMP and SSAMP, as well as for PINIT and SINIT.

We will start by adjusting the PSAMP and SSAMP times, beginning with $155\mu s$ and increasing the time $15\mu s$ per iteration, while keeping PINIT and SINIT fixed at $24\mu s$. The results are presented in Table 3.6, which indicates that the optimal value for PSAMP and SSAMP is around $185\mu s$.

PSAMP = SSAMP (μs)	155	170	185	200	215
Std. dev.	6600	6050	4870	5300	5420

Table 3.6: Standard deviation for the different PSAMP and SSAMP times.

Then, we will optimize the PINIT and SINIT times, starting at $20\mu s$ and increasing the time $4\mu s$ per iteration, with PSAMP and SSAMP fixed at the optimized time of $185\mu s$. The results are shown in Table 3.7, where the optimal value is found to be between $24\mu s$ and $32\mu s$, with $28\mu s$ chosen as the optimal value. Comparing both tables, we can observe than the CDS technique is more sensible to variations in PSAMP and SSAMP times rather than PINIT and SINIT times.

PINIT = SINIT (μs)	20	24	28	32	36
Std. dev.	12200	10460	10400	10800	12300

Table 3.7: Standard deviation for the different PINIT and SINIT times.

3.3.6 Skipper images

Once we found these optimal parameters, we wanted to take images with skippers. The current standard deviation is around 2600, when doing skippers, we expect the noise decays with the square root of the number of the skips, as in Figure 1.8. When we take images with different number of skips, first with 500 skips, the standard deviation reduces almost a half, 1400. The problem is that now, glowing starts to appear, inducing more charge. With 1500 skips, Figure 3.8, the standard deviation increases again, reaching 2000.

This increase in standard deviation happens because, as the noise decreases with the number of skips, the pedestal value is reduced. When glowing induces low-energy charges, a higher pedestal without skips makes it difficult to observe this effect. However, with the reduced pedestal due to the skips, these previously obscured charges from the glowing become visible, contributing to increase the standard deviation. Additionally, the reduction in the pedestal makes previously hidden defects in the silicon, such as hot columns, more visible.

These issues make it impossible for us to work with skipper images, which are the ones used for a physical analysis because of its single electron resolution.

Parameters optimized

The optimal values for the parameters we have studied are in table 3.8.

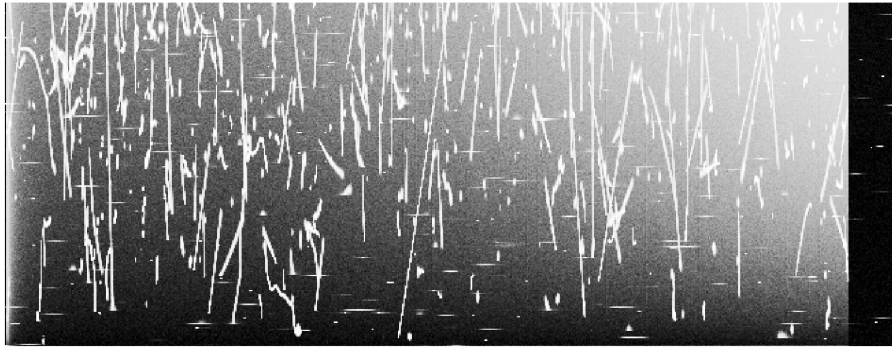


Figure 3.8: *Image taken with 1500 skips.*

Parameter	Low Value (V)	High Value (V)	Time (μ s)	Voltage (V)
Horizontal gates	−0.5	2.5		
Vertical gates	−1	4.5		
Bias voltage				45
PSAMP, SSAMP			185	
PINIT, SINIT			28	

Table 3.8: *Optimal values for the parameters.*

At this point, we have not been able to take high quality images in order to carry out a physical analysis as planned initially, mainly due to the glowing we have. However, we have made significant progress in reducing electromagnetic noise, particularly thanks to the improvements in grounding.

The setup has now been moved to the LSC at Canfranc for radiopurity studies, where right now the CCD PP52 is installed. Additionally, new CCDs will be purchased for future characterization, with the expectation of acquiring scientific-grade CCDs similar to those installed in the LBC.

Chapter 4

MOSKITA

4.1 Introduction

As we said before, the images provided from the setup at IFCA were not as good as we desired and any type of physical analysis can not be done with them. For the second objective proposed in the TFM, the design and implementation of an automatic muon detection algorithm, we will use the images provided by the MOSKITA (MOBILE SKIpper Testing Apparatus) experimental setup. In fact, the MOSKITA setup is very similar to the one at IFCA, as shown in Figure 4.1(a). The detector is a skipper-CCD with dimensions 6144×1024 pixels. Every pixel is $15\mu m \times 15\mu m$. Then, the physical dimensions of the CCD are $9.22cm \times 1.534cm$. For readout, it also has four amplifiers, but only three of them work and only two are used for scientific analysis. From now on, the useful amplifiers will be called amplifier 2 and amplifier 3. The temperature at which the CCD works is about $140K$, $20K$ higher than at IFCA, and it has a pressure of $10^{-6}mbar$.

This setup is located at the milliQAN site [18] at the Large Hadron Detector (LHC) [17]. It is located in a tunnel 70 metres underground, which reduces the cosmic ray muon flux by a factor of ~ 100 compared to the surface. It is ~ 33 m away from the CMS interaction point. Between MOSKITA and the CMS interaction point there is ~ 17 m of rock, which will shield the detector from most of the particles produced in the collisions. We expect that a fraction of the muons produced at the interaction point will escape and reach us, so we are interested in detecting them. In the CMS coordinates system, the detector is positioned at an azimuthal angle (ϕ) of 43° and a pseudorapidity (η) of 0.1. In figure 4.1 we have a diagram of the position of MOSKITA.

The main objective of MOSKITA is to go beyond the DM scenario by exploring the existence of millicharged particles (mCPs), hypothetical free particles that would have a charge much smaller than the elementary electron e^- . Scenarios beyond the Standard Model of particle physics can naturally include particles [22, 26], whose electric charge is a small fraction of the electron's charge. In particular, the mCPs can be considered as well-motivated dark-matter candidates [23–25]. The simplest way to introduce mCPs in a model is to consider them as a

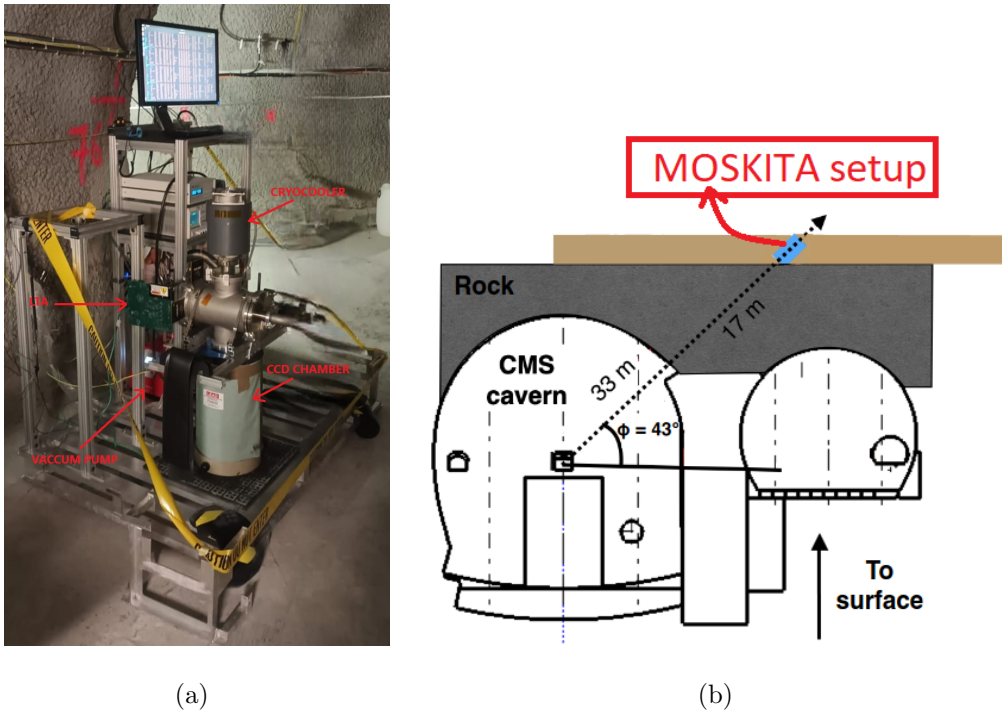


Figure 4.1: (a) Setup of the MOSKITA setup placed in one of the LHC tunnels. (b) Longitudinal view of the location of the MOSKITA setup at the LHC. Figure from [20]

low-energy limit of the theory, where a hidden (dark) photon kinetically mixes with the visible standard model photon. As a result, e.g., a new fermion of the hidden sector, coupled to the hidden photon, can acquire a small electric charge. The mass range for the main theories of mCPs, goes from the MeV to GeV.

mCPs could be produced from cosmic rays in the Earth's upper atmosphere [27], but they can also be produced in high energy collisions at particle accelerators. That is why we are interested in placing a detector near the interaction point of an accelerator. MOSKITA, while similar to DAMIC-M and OSCURA in being a direct detection experiment, specifically aims to detect mCPs produced from proton-proton interactions. This focus on accelerator-generated mCPs introduces a distinction from the other experiments.

The MOSKITA setup was located at the Fermilab in the MINOS underground hall [19] before it was transported and shipped to the LHC. This first experimental setup at MINOS [20], as part of the SENSEI collaboration, showed that the single electron resolution using skipper-CCD technology, allows new constraints to be placed on the mCPs as DM candidates in the MeV mass range. With the new site in the LHC cavern, the collaboration plans to measure the low-energy background at the site during beam-on and to evaluate the feasibility and better estimate the scientific range of a large skipper-CCD array for dark sector searches at CERN. Furthermore, the energy involved in the NuMI beam at MINOS is relatively low energetic, so the production of GeV-mass mCPs is highly suppressed. But the beam energy of the LHC is far more energetic than the NuMI beam, this provides an opportunity to further probe the

mCPs parameter space in the GeV mass range.

As previously mentioned, the objective of MOSKITA is to assess the background and study the feasibility of such measurements. One of the key points, is to distinguish the cosmic particles from those produced as a result of the interaction. For example, muons can be separated based on their angular distribution, that of the CMS interaction point.

As a first step, create an algorithm to differentiate muons from other particles will be useful.

The second objective of the TFM, is to create an automatic muon detection algorithm using a deep neural network. This objective is doubly motivated. Within the framework of MOSKITA, we want to verify that there is a fraction of particles that come to us with a privileged direction, such as that from the CMS interaction point. We will do this by studying muons, since, as we will see later, muons are the only particles that pass the detector in a straight line, so we can study its direction.

Outside the MOSKITA framework, in DAMIC-M we are interested in detecting muons because they are the most common particles to define diffusion. As muons pass through the detector, entering from one side and exiting from the other, they generate holes throughout the CCD's bulk. This process allows for the modeling of diffusion as a function of the depth within the CCD.

Once the algorithm is completed, the idea is to integrate it into WADERS, the official software of the DAMIC-M collaboration to process data.

For this part of the work, we will be using data which started to be taken from the 15 of March 2024. For this data, there were no collisions at the LHC, the first stable beams started the 8 of April, and the collisions with 1200 bunches started the 25 April [16].

To extract meaningful information from the raw images taken by MOSKITA, we must perform a cleaning process first. This involves removing the pedestal and filtering out malfunctioning columns, rows, or pixels (called hot columns or pixels). Calibration and clustering processes are then applied to obtain the charge distribution of each pixel, which provides the actual image captured by the detector. In Section 4.2, we will explain these processes in detail. We optimized the identification of hot columns by creating an automatic script to handle this task, see Section 4.3.

Once the images are cleaned and clusters identified, we are ready to work with our DNN. We will need to select tracks originating from particles to train our neural network, as described in Section 4.4.

Finally, in the last section, after training our neural network, we will use it to investigate whether the number of muons increases with LHC luminosity, as discussed in Section 4.5.

4.2 Data Cleaning

We will utilize WADERS, the official software provided by the DAMIC-M collaboration to do the different steps to process the image from the cleaning to the clusterization. This

software facilitates data processing by performing a series of operations on each image. The images will be processed through the following certain steps sequentiality:

- Compress Skipper Process: As explained above in the skipper technology, read the same pixel several times improves the readout noise by taken the average of all the measurement. this process allows to do this average. The MOSKITA takes 169 measurements (skips) of the same pixel getting a readout noise of $0.19e$.
- Pedestal Subtraction Process: The purpose of this process is to subtract the pedestal, which is an arbitrary offset added to avoid negative charge readings. This brings most pixel values to their real value, which has to be zero except for those pixels with charge. The width of this distribution around zero is the electronic noise. In Figure 4.2(a), we have the value of the pedestal vs rows. The decrease seen is very small and will be corrected with the pedestal subtractions. In Figure 4.2(b), we show the sigma values per row. The sigma values do not vary significantly, indicating that the noise remains consistent across the rows.
To ensure accurate baseline estimation, we first exclude outlier pixels, typically associated with particle tracks, as they could distort the baseline. After removing these outliers, the remaining pixel values should follow a Gaussian distribution centered around the baseline. The pedestal is then calculated as the mean of this distribution.
- Cluster Finder: This process is responsible of identifying the particles tracks found in the detector. The clustering algorithm identifies energy deposits from particles by locating pixels with charge above a user-defined threshold. It begins by identifying at least one pixel, known as the seed, with the highest energy. Adjacent pixels are included if they also meet the energy requirement. This process enables further studies with the detected particles.
- Build Cluster Mask: This process is a continuation of the previous one. Once the cluster are identified, a mask is created to cover them, ensuring they are excluded for further analysis. This process is essential to calculate the gain and the dark current as we only study the background.
- Apply Selection Cuts: This process allows for the exclusion of certain areas when analyzing the data. It can be useful for focusing on specific regions, such as the overscan, or for omitting defects in the CCD, such as small glowing areas or silicon imperfections. See a detail explaination in Section 4.3.
- Fit Dark Current Process: This is the final process applied, where the charge pixel distribution is fitted to determine the gain and dark current. While determining the dark current is crucial, as it represents one of the limiting factors in the search for Dark Matter, it is not relevant for our purpose of identifying muons. For our analysis, we are only interested in determining the gain. With the gain value, we can convert from Analog-to-Digital Units (ADUs) provided directly by the detector to electron units by dividing the pixel value by the gain. The histogram is modeled using a Gaussian function convoluted with a Poisson distribution, fitting the first two peaks, where the impact of ionizing particles is minimal due to their high energy.

In Figure 4.3 we show an example of this fit, along with the calculated values for the gain and the dark current (λ) for a given image. The gain is the difference between the first and second peaks. The first peak represents events with no charge, while the second peak

corresponds to events with one electron charge. To calculate the readout noise, we divide the sigma of the first peak by the gain. The blue points in the figure represent masked clusters, which were excluded from the fit.

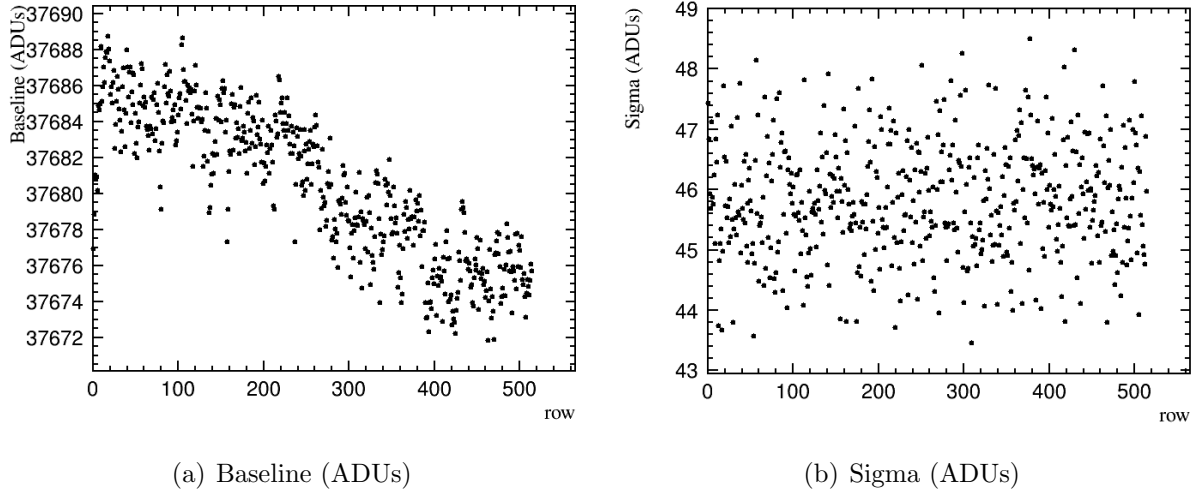


Figure 4.2: Example of the Pedestal Subtraction Process for the image number 15 from the data that started the day 15 of March 2024.

For each image taken during the run and for each amplifier separately, the gain and dark current are calculated using the previous steps. Figures 4.4, 4.5, 4.6 and 4.7 show the values plotted against the images over time. It can be observed that these values remain constant, so they are fitted to a constant value and the same value is used for each amplifier. The results are presented in Table 4.1, where the readout noise for both amplifiers is calculated, approximately 0.19e for amplifier 2 and 0.2e for amplifier 3.

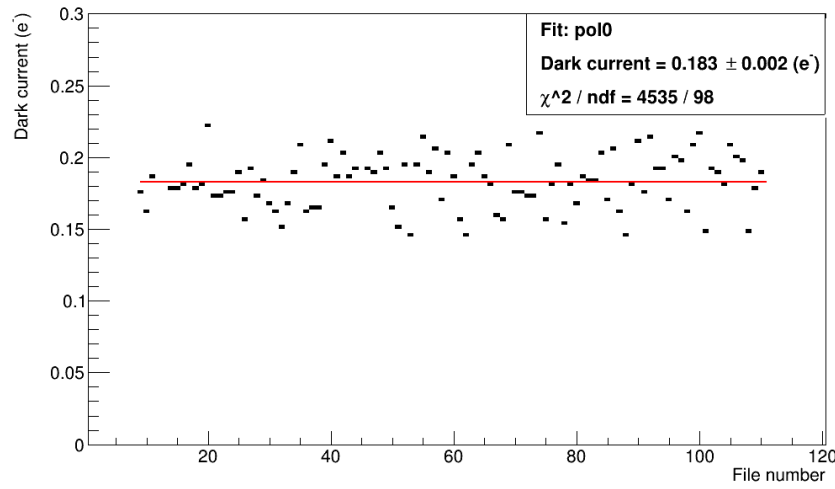


Figure 4.4: Dark current histogram fitted into a constant for the amplifier 2.

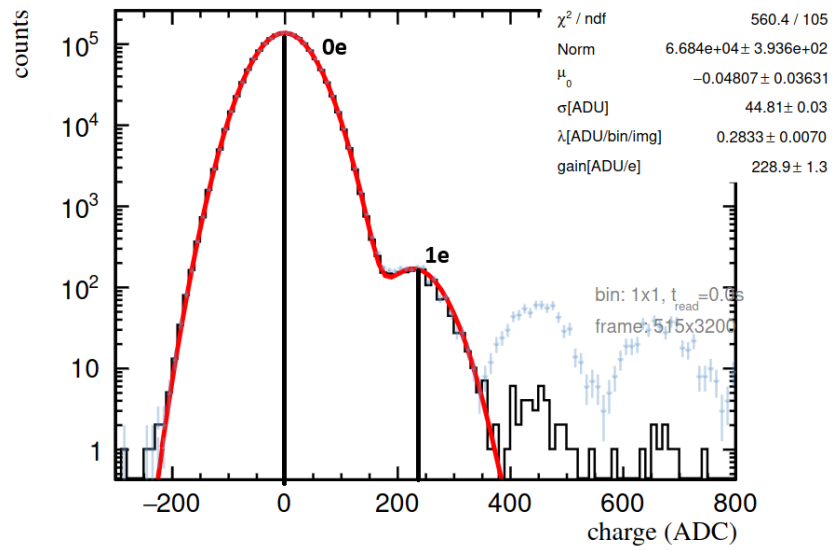


Figure 4.3: Example of the output for the Fit Dark Current Process process for the image number 15 from the data that started the day 15 of March 2024.

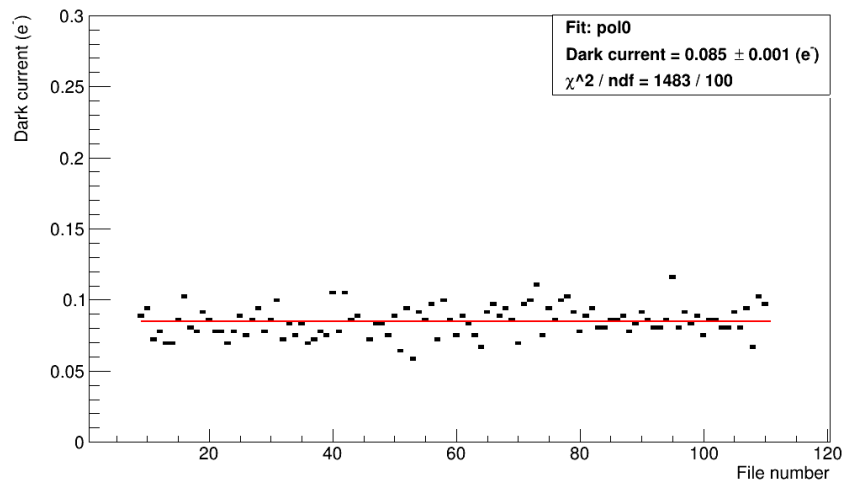


Figure 4.5: Dark current histogram fitted into a constant for the amplifier 3.

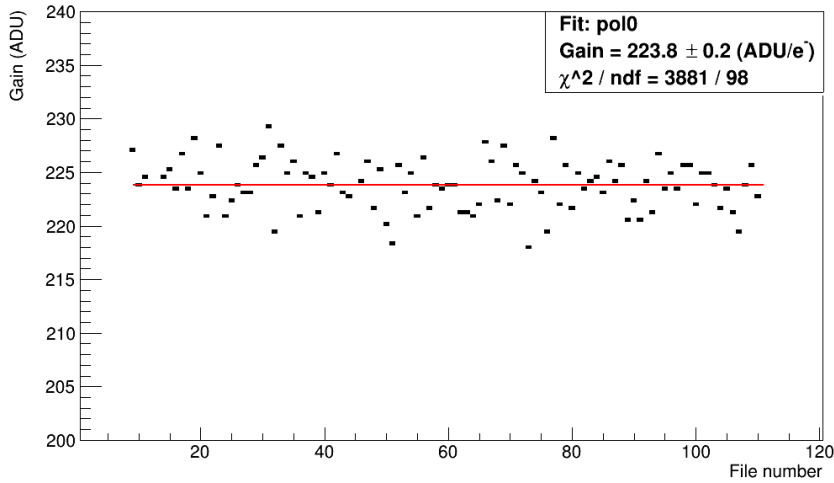


Figure 4.6: Gain histogram fitted into a constant for the amplifier 2.

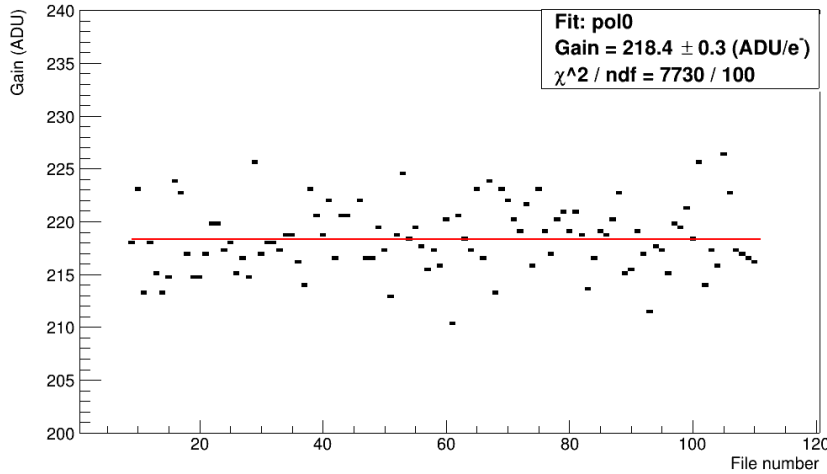


Figure 4.7: Gain histogram fitted into a constant for the amplifier 3.

Amplifier	Dark current (e^-)	Gain (ADU/ e^-)
2	0.183 ± 0.002	223.8 ± 0.2
3	0.085 ± 0.001	218.4 ± 0.3

Table 4.1: Dark current and gain for the different amplifiers using the images from the 15 of March 2024.

Once we have our data cleaned and calculated the gain and dark current, we are ready for the next step. These images have been removed from clusters but not from hot columns and pixels, which could distort their values. In the next section, we will develop an automatic algorithm to clean these defects.

4.3 Hot Columns

Hot columns, cold columns, and hot pixels are caused by defects in the silicon net or crystal of the detector. These defects create wells where charge accumulates, injecting “fake” charge values into the CCD and distorting the image. Identifying these defects is crucial for accurately estimating dark current, gain, and noise, as well as removing additional background when extracting the Dark Matter signal. This section describes a method that automatically detects hot columns, cold columns, and hot pixels, allowing us to mask them and exclude them from the analysis.

Figure 4.8 shows an example of hot columns. Columns affected by defects can lead to incorrect results for the dark current. Dark current events typically have charges between $1e$ and $3e$. However, defects in the silicon, such as hot columns, can also “generate” events within this energy range. Consequently, when reading the CCD, we might include events that are not due to dark current. These defects decay exponentially [29]leaving charges in the next columns. During the Cluster Finder process, these events are left under the radar as they do not meet the seed/ pixels requirements.

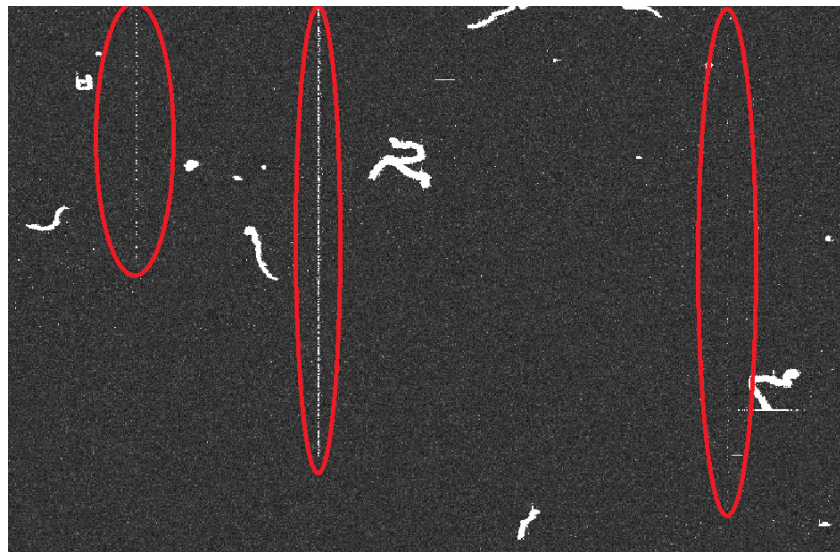


Figure 4.8: Image number 76 from the 15 of March 2024 from the MOSKITA setup with 3 visible hot columns.

We merge all the images for each amplifier to enhance the statistical data and identify hot columns. We extract the number of events collected in each column across all images. Hot columns will exhibit a high number of events, as they accumulate charges between 0 and $3e$. By combining all the images, we improve the statistical data, resulting in more pronounced peaks in these hot columns.

We will plot the number of events with charge between zero and three electrons, to avoid particle events, grouped by column. If there were a hot column in the detector, it would

continuously inject events into the same column, resulting in a spike in the affected columns.

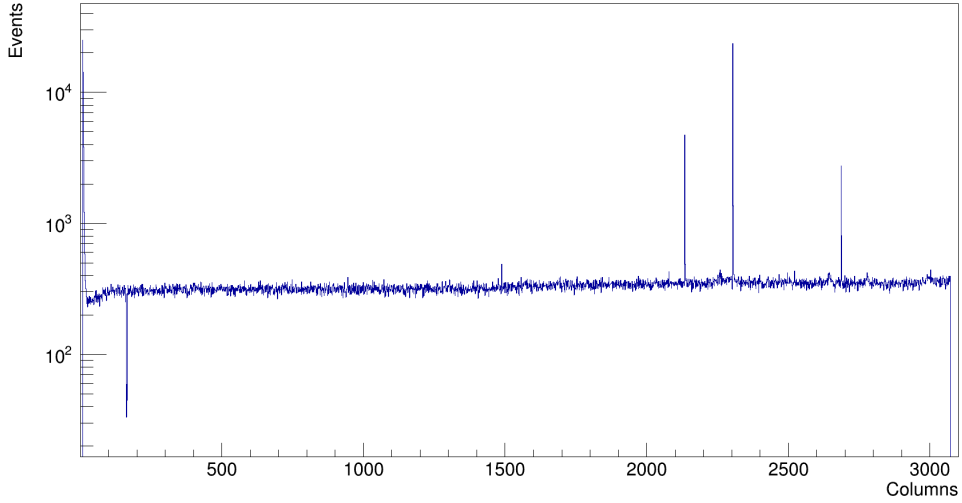


Figure 4.9: Number of events with charge between 0e and 3e per column for amplifier number 2.

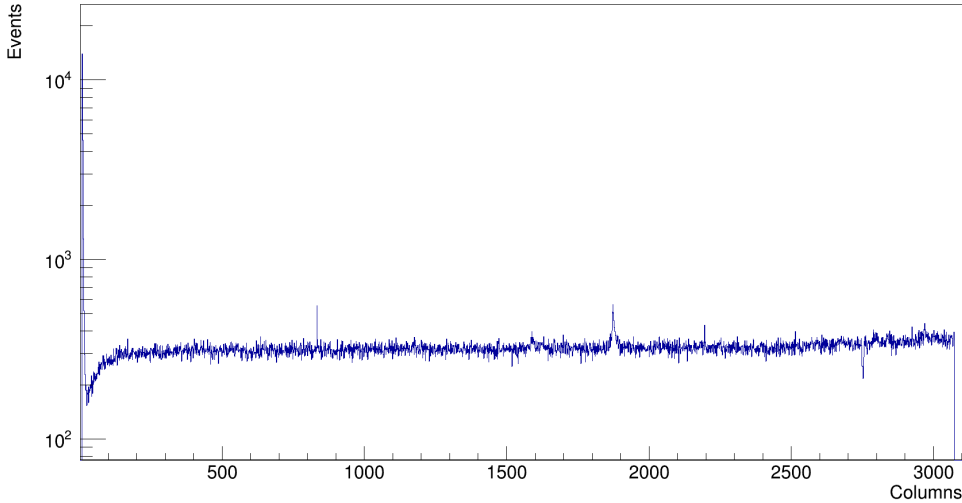


Figure 4.10: Number of events with charge between 0 and 3e per column for amplifier number 3.

The histograms are depicted in Figure 4.9 for amplifier 2 and in Figure 4.10 for amplifier 3. In Figure 4.9, we can clearly see some hot columns, also notice that appears some columns which show a defect of events, “cold” columns. For amplifier number 3, shown in Figure 4.10, the hot columns are not as pronounced as in amplifier 2, but they are still discernible. This observation suggests that, rather than an entire column being defective, the defects may be partial, affecting only a portion of the column. As shown in Figure 4.8.

Find these defects automatically following a criteria define previously rather than having to look one by one is more objective and precise.

The idea we followed was to first fit the number of events with charge between $0e$ and $3e$ per column to a first order polynomial. We will start the fit after the first 20 columns, which are usually with more defects. Then, we calculate the standard deviation, or sigma, between the 10% and 90% percentiles to get rid of the events with very low and high values.

Once we have our sigma calculated, values outside a 4 factor of sigma, are the ones that are going to be considered as hot columns. Plotting the histograms with the polynomial fit and the 4σ lines, we get:

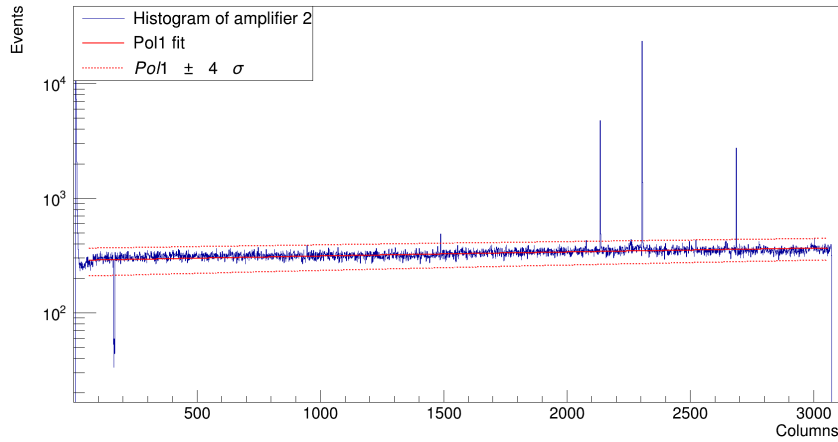


Figure 4.11: Number of events with with charge between $0e$ and $3e$ per column with, the fit into a first order polynomial and the regions to determine if it is a hot column for the amplifier number 2.

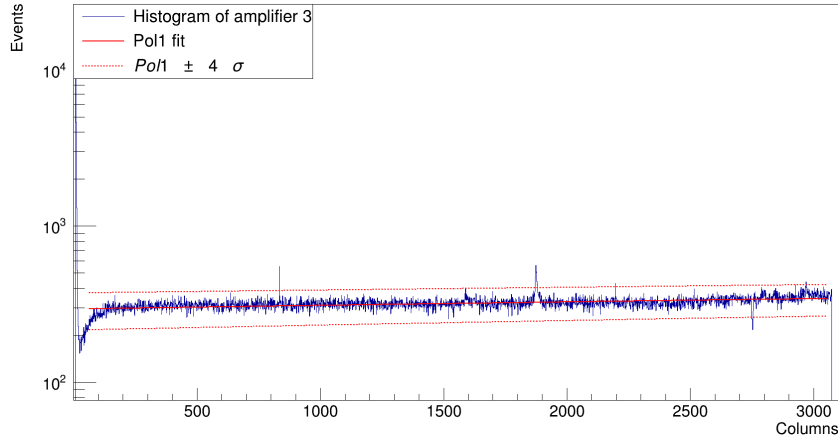


Figure 4.12: Number of events with charge between $0e$ and $3e$ per column, with the fit into a first order polynomial and the regions to determine if it is a hot column for the amplifier number 3.

As we can see in 4.11 and in 4.12, this is a good way of automatically finding the hot columns in our CCD. This script was written with the intention to be added to the WADERS

software as an update, so the main output that we get from the script is a list containing the hot columns in the WADERS format. So once we find the hot columns we just have to copy and paste them into a process called Apply Selection Cuts to ignore them.

Now, we will focus on what appears to be a cold column, located around column 200 in Figure 4.11. By zooming in on this region, as seen in Figure 4.13, we observe that these columns have approximately five times fewer events than others. Additionally, we notice that the events in these columns do not follow an exponential as we said at the beginning of the section.

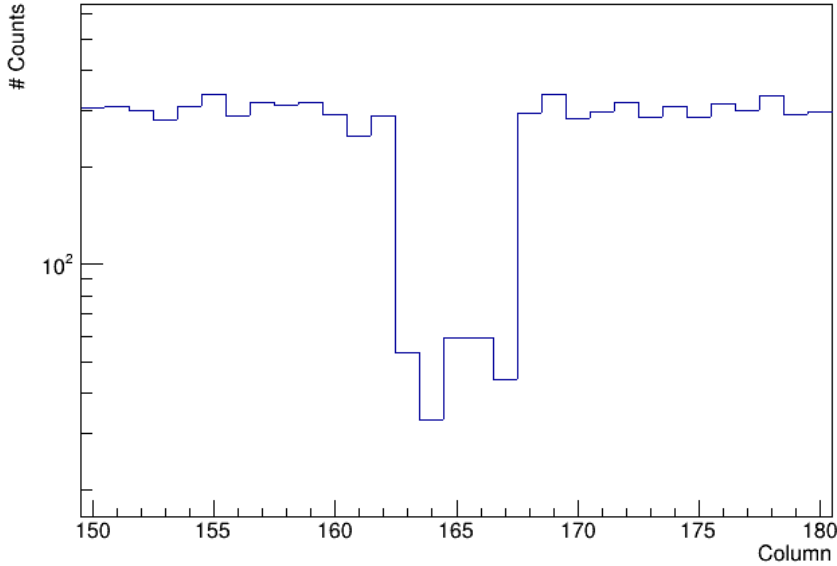


Figure 4.13: Zoom into an apparent cold column from the number of events with charge between 0e and 3e per column for the amplifier number 2.

Next, we will plot the numbers of events with any charge per column. This histogram should also follow a first-order polynomial due to all the statistics we have. In the case of a hot column, we expect to see a peak. The histogram of the number of events per column is depicted in Figure 4.14. Around column 200, where we previously identified the cold column, we now see a peak, indicating the presence of a hot column. This hot column appears to be injecting charges with charges higher than 3e, rather than the low energy charges typically seen in other hot columns.

The main work for this script has been done, but it is still not finished because we have chosen that to be a hot column, the number of events must deviate from the fit line 4σ . We need to find the best value to consider a hot column.

We are going to merge all the fit files one above the other because hot columns do not change their position. We will also need a text file with the number of columns and how many sigmas the column deviates from the linear fit, we get this with the previous script. First, we are going to create an initial mask that includes the clusters that have seed and events that have an energy other than 0e to 3e electrons. Then we will start with a high sigma value and

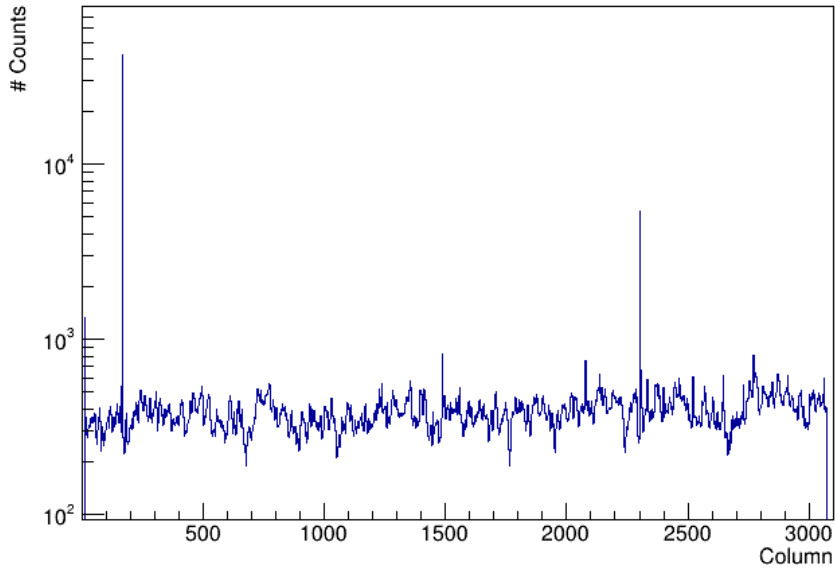


Figure 4.14: Number of events with any charge per column for the amplifier number 2.

reduce it to a minimum value of 2σ , and keep adding to the initial mask the columns that have a deviation higher than the sigma. We are going to plot the number of events with charge between $1e$ and $3e$ electrons divided by the number of columns, which is like a density, versus the sigma. In this way, we expect the number of events produced by the hot columns to be minimised and then a step decrease to zero for smaller sigmas. In Figure 4.15, we can see that the sigma that optimizes the number of events is 3, a value really close to 4, the one we use previously.

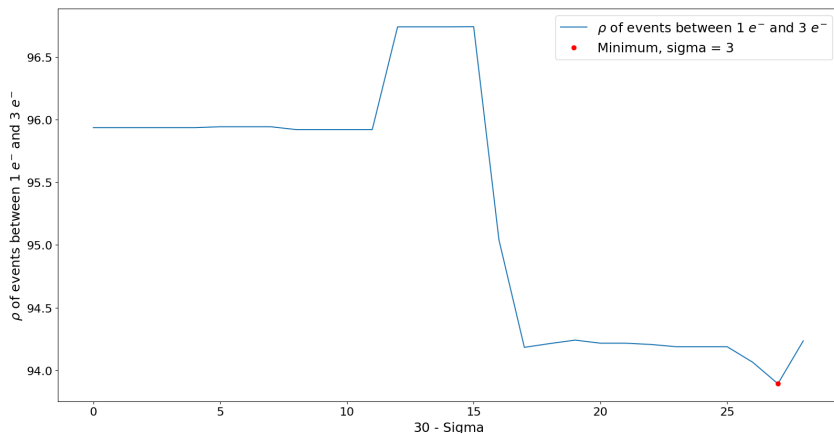


Figure 4.15: Density of events with charge between $0e$ and $3e$ vs the sigma for the amplifier 2.

4.4 Particle Classification

The last part of this work is going to be the creation of a Deep Neural Network (DNN) capable of classifying clusters depending on the type of particle that produces them. The objective of this DNN is to automatically classify the different types collected in the detector for different analysis such as diffusion studies. For this, we are going to use the YOLO (You Only Look Once) object detection and image segmentation model developed by Joseph Redmon and Ali Farhadi at the University of Washington in 2015. The most recent stable version and the one we are going to work with, is with the YOLOv8. YOLO allows training DNNs for various purposes like detection, segmentation, and classification, and in this case, we are specifically interested in its classification capabilities. Also, there are different neural networks architectures starting from simple architectures to highly complex architectures with tens of millions of parameters.

To train the DNN, we first need to create a dataset with cluster images from the different particles we want to classify. The idea is to create a DNN that is able to classify muons, electrons, alpha particles, serial register events and hot columns. The training images come from those captured starting on March 15, 2024, which have been used throughout this chapter.

To obtain the cluster images, we need to determine the energy at which pixels saturate in each amplifier. This is achieved by plotting a histogram of the number of events versus energy, as shown in Figure 4.16. We can observe that amplifier 3 saturates at 5keV , which is problematic because events energies higher than 5keV cannot be detected in this amplifier. This issue was notified to the scientists responsible for the setup, and it was solved by adjusting some CCD parameters as we did in Section 3. Therefore, we will only use the clusters from amplifier 2. Note that this issue was resolved for images taken starting on May 22, 2024.

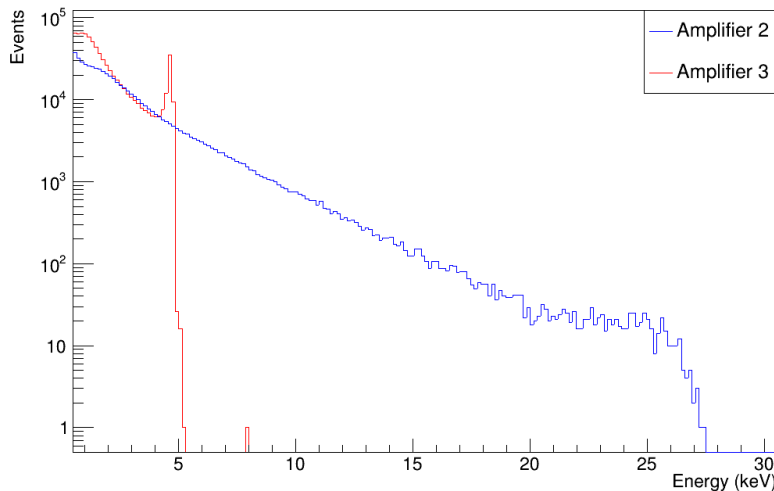


Figure 4.16: Saturation energy per pixel in the CCD per amplifier from the images taken the 15 of March 2024.

Now, we can obtain the cluster images from the root files using WADERS. Once we have the image of the different clusters, we will create a dataset and manually classify the clusters

based on the type of particle they represent. The different particles we will classify are:

- The alpha particles have a circular shape, which topologically is very similar to a two-dimensional Gaussian, called “plasma”, Figure 4.17(a). Plasma alphas are originated in the bulk or close to the back of the CCD, their appearance is due to the high diffusion. But in contrast, if the alpha originates near the front of the CCD, alphas can produce elongated tracks in the columns because the charge spills between the adjacent columns. This type of alphas are called “bloomed” alphas, Figure 4.17(b). Furthermore, alphas are very dense because its energy is of the order of ($\sim MeV$). The alpha particles mainly come from the disintegration chains from the Uranium 238 and Thorium 232 [31], mainly from the Radon 222 and Thorium 228 that are present in the air. Also, their penetration is very limited, that is why they look like a circle.

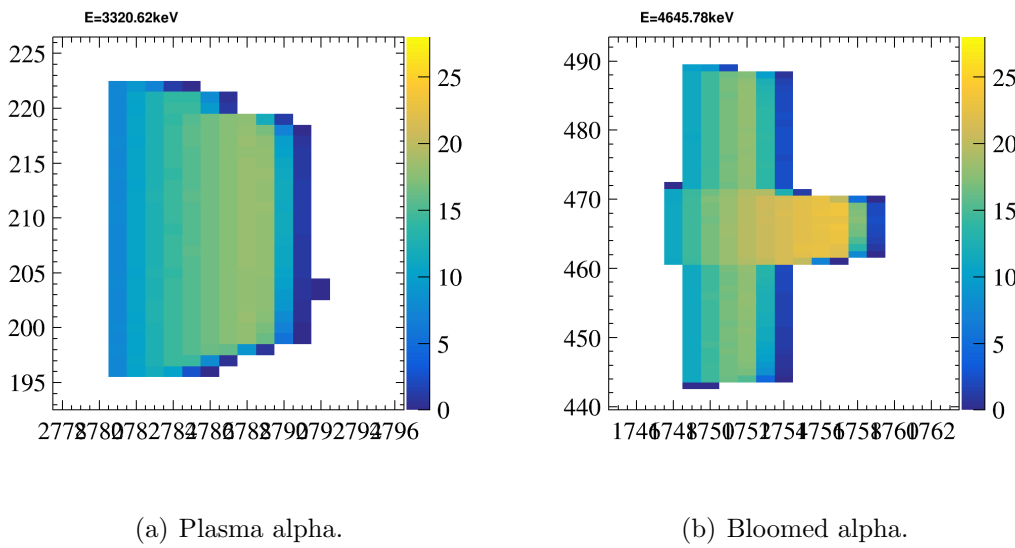


Figure 4.17: Different types of alphas.

- Next, we have the electrons 4.18 or betas if they come from nuclear disintegration. Depending on its energy, can look in three different ways, it can look like a point-like event or with a small tail if the electrons have low energy 4.18(a). Generally, electrons with energy lower than $130 - 150 keV$ look like this. If the electron has the sufficient energy, it will move through the detector while suffering scattering with the different particles of the detector till it “dies” in the detector and leaves the Bragg peak, the maximum energy deposit for massive particles after they completely stop. These movements will be seen in the detector as a winding track, commonly referred to as “worms” 4.18(b). These electrons come from either Compton scattering or beta decay. Finally, if the electron is very energetic, it can go through the detector without stopping, we would not see the Bragg peak and will be very different to distinguish from a muon. These “super” energetic electrons come from cosmic rays, these events are very rare. Furthermore, an energetic electron can also create another electron, which is called a “son” electron.

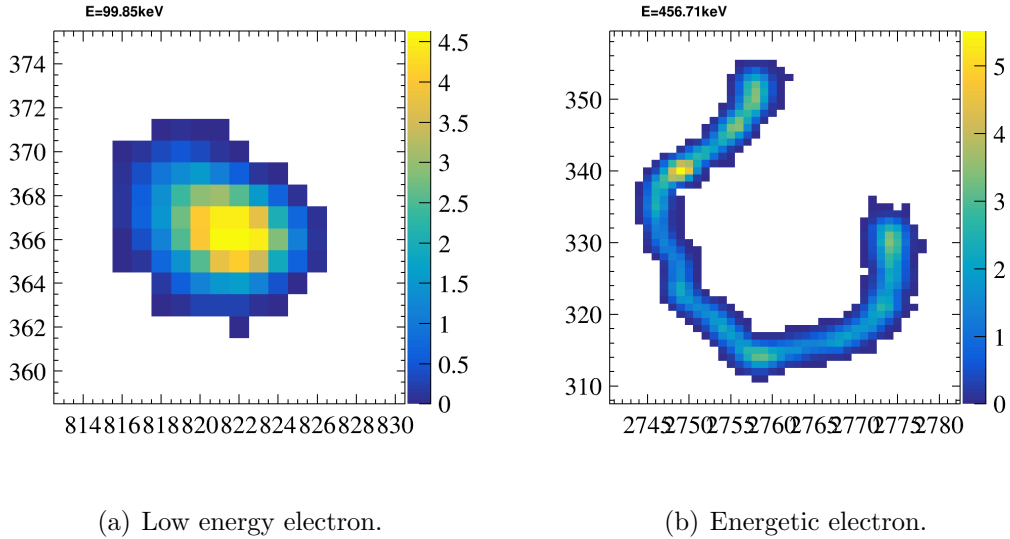


Figure 4.18: Different types of electrons.

- We also have muons 4.19, the muon is a very easy particle to differentiate because it resembles the shape of a baseball bat. It is more massive than the electron but not as massive as the alpha nuclei so it does not suffer scattering with the detector and unlike the electrons, the muons do not “die” in the detector, they go through the detector. They also deposit the energy in a constant way. Most of the muons come from cosmic rays, but in this setup we are relatively near to the CMS interaction point, so we also expect that there are incoming muons with a privileged direction when the beam is on. In some images the muon can appear a bit bent because in the detector exists a small magnetic field.

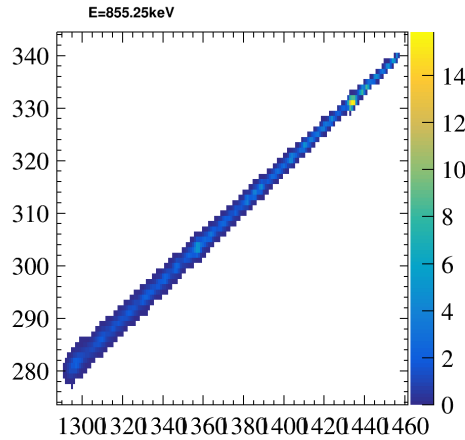


Figure 4.19: Muon.

- Moreover, we are also going to add hot columns 4.20, because sometimes if a particle passes next to a hot column, the hot column can also be clustered with the particle, so

the total energy of that particle will not be the real energy from that particle and we do not want to cluster these type of events.

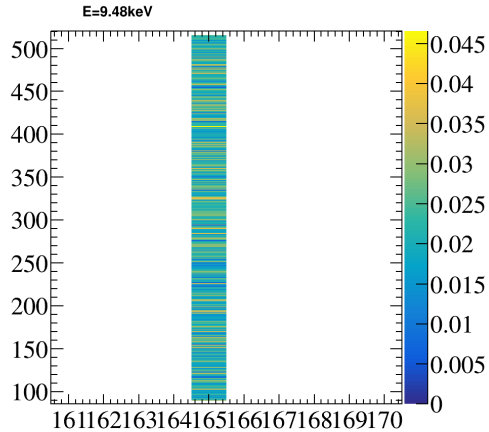


Figure 4.20: *Hot column.*

- In a similar way, we are going to look for serial register events 4.21 is a particle that passed at the same time when the serial register was been read and it is not a valuable cluster.

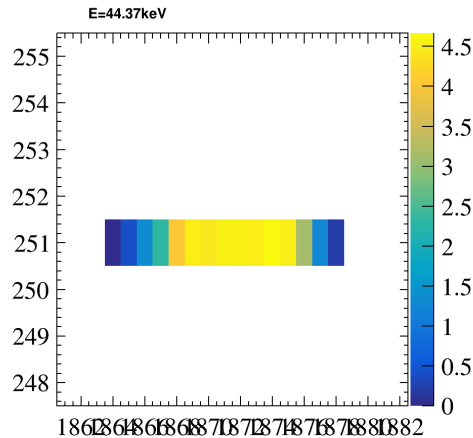


Figure 4.21: *Serial register event.*

- Last but not least, we are going to include the detection of multiple events 4.22. Here we include the combination of two or more particles.

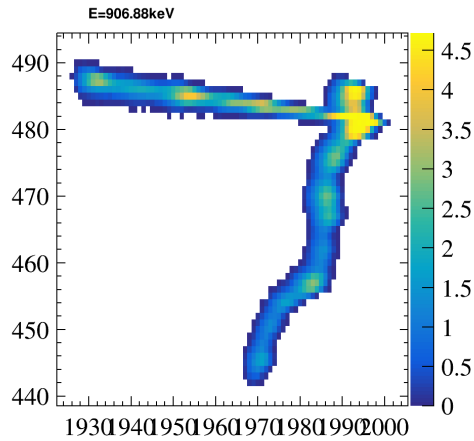


Figure 4.22: Multiple event of a muon and an electron.

When creating the dataset for the training, I encountered a problem with finding alpha particles. Despite analyzing nearly 12000 cluster images, I could not find any alpha particles. The events that resembled circles, were low energy events, likely electrons or other low-energy particles, rather than alphas.

To address this, we will use the root files to look for events that have an energy higher than 1MeV , to exclude low energetic clusters that look like alphas, and that its pixel density is higher than 0.6, to exclude muons that deposit a lot of energy. Pixel density is the division between the number of pixels by the area of the rectangle that contains the cluster. For alpha particles, this pixel density is a circle inside a square, the expected pixel density is $\pi/4 \approx 0.79$. Despite this approach, we did not find any events meeting these criteria. We plot pixel density against energy to further analyze the data, as shown in Figure 4.23.

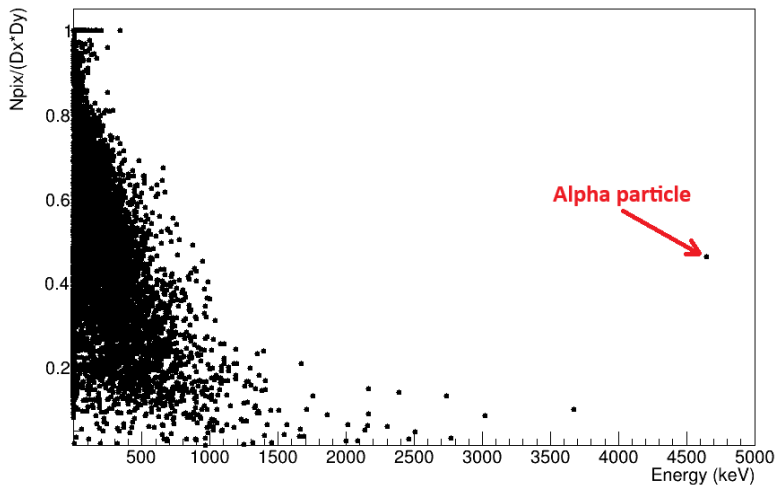


Figure 4.23: Pixel density versus the energy of the cluster. Clusters from the 15 of March 2024, amplifier 2.

In the plot shown in Figure 4.23, we observe a point that nearly satisfies our criteria for an alpha particle. That point corresponds to a bloomed alpha and is depicted in Figure 4.17(b). Additionally, we notice events with a pixel density of one, which could indicate serial register events, hot columns or single pixels.

Due to the limited number of alpha particles, we will also examine events from amplifier 3. Although we initially avoided using this amplifier due to pixel saturation issues, the primary difference will be in the color of the pixels. We hope that the DNN can learn to classify particles based on the shape, without relying on pixel color. In total, we only identified two alpha particles in this set of 13000 images. This scarcity may be due to the location of MOSKITA, where alpha particles are absorbed by the surrounding rocks.

Once we have classified the images depending on the type of particle it is, we will split the images in two sets: 80% for training the DNN and 20% for validation. Additionally, YOLO has automatic data augmentation techniques to increase the dataset. These techniques include altering colors, adjusting saturation, rotating, and flipping images, among other modifications.

Once the dataset is ready, we will start training two different classification models, and use the one with better results. The first model is the basic one, “YOLOv8n-cls” with $2.7M$ parameters, which we will refer to as the “simple” DNN. The second model is more intricate, the “YOLOv8s-cls” with $6.4M$ parameters, which we will refer to as the “complex” DNN. Instead of building the models from scratch, we will load pretrained versions, as recommended by the ultralytics documentation. We will train the DNNs for 300 epochs, with a patience of 15% (45 epochs) to prevent overfitting. The hyper-parameters will be the default ones.

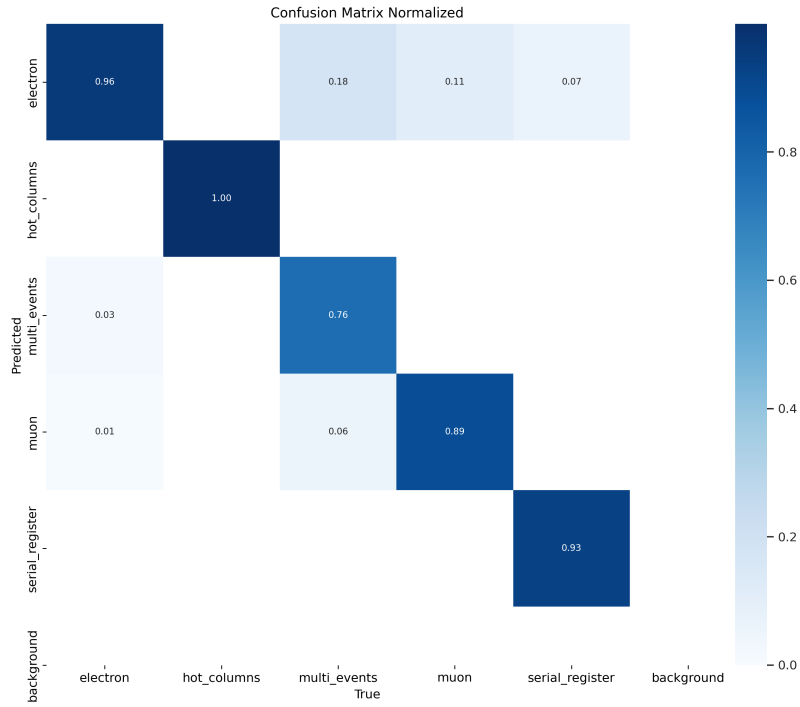
Once training is completed, the software will automatically classify the validation images, providing us with a confusion matrix. By comparing the normalized confusion matrices of both models, we can determine which DNN performs better and use that model for further analysis. The confusion matrices for both DNNs are presented in Figures 4.24(a)-4.24(b). Calculating the trace of both matrices, the simple DNN has a trace of 4.54, meanwhile the trace for the complex is 4.52. The simple DNN seems to work slightly better.

There are some images of the prediction of the DNN in Appendix 4.5

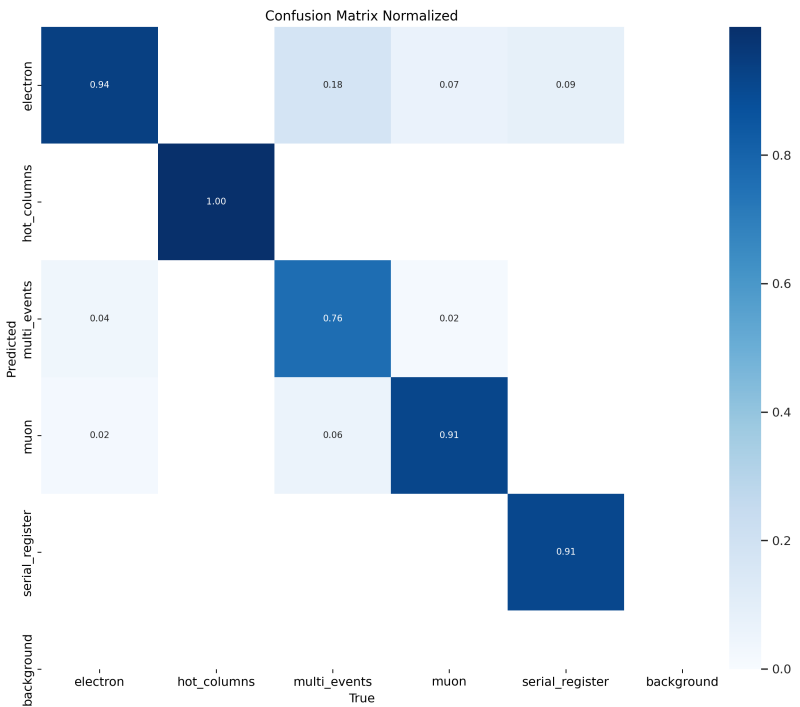
4.5 Number of Muons Per Day

Once we have the DNN trained, we are going to use it to check if whenever the luminosity of the LHC increases, the number of muons also increases. In this section we will use data collected on 13 May 2024, in this data we have periods of high luminosity and periods of no luminosity. With the DNN we are going to obtain the number of muons per image, file. Then, in the root files of the images, there is a new branch containing the variable “pp_proc”, that is related with the luminosity of the LHC. Finally we will plot the number of muons per file number and superposed, the luminosity per file number.

This plot is in Figure 4.24, as we can see, with this dataset, the number of muons does not increase proportionally with luminosity as expected. This may be because the CCD is very



(a) Simple DNN confusion matrix normalized.



(b) Complex DNN confusion matrix normalized.

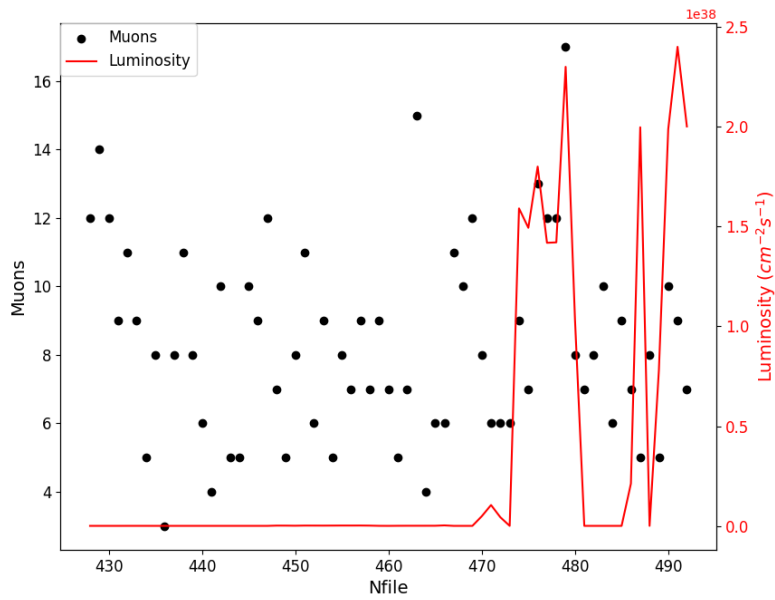


Figure 4.24: Number of muons and luminosity versus the File number.

small, resulting in a small solid angle for the muons to go through the CCD, which leads to a low probability of muons arriving the CCD.

Conclusions

In this Master's thesis, we explored dark matter detection and various search techniques, focusing on direct detection using CCDs and the innovative Skipper-CCD technique. We characterized the IRONMAN experimental setup at IFCA with new readout electronics, LTA. Although we could not fully optimize the setup due to CCD quality issues, we achieved a twofold improvement in electromagnetic noise by enhancing the grounding and connecting all instruments to a new UPS. These CCD issues prevented us from using WADERS, the standard software for such characterizations, and conducting additional tests. The experiments indicated that the CCDs are nearing the end of their useful life, emphasizing the need for new CCDs.

We utilized data from the MOSKITA setup at the LHC to search for milicharge particles. This setup, which uses Skipper-CCDs similar to those at IRONMAN and also employs the LTA readout system, provided data from March to May 2024. We employed this data to develop an automated algorithm for detecting hot columns and identifying muons. Muons, a significant background at MOSKITA, need to be distinguished from the signal of interest to avoid contamination from cosmic rays. Additionally, we developed a script for the automated identification of silicon defects, such as hot columns, and created a Deep Neural Network (DNN) to differentiate between various types of particles arriving at the detector. This DNN will be integrated into the DAMIC-M collaboration's official software, WADERS, for future analyses, particularly for studying diffusion. Using this DNN with data from the MOSKITA setup, we found that the number of muons arriving at the setup is not proportional to the LHC luminosity.

Future work

For future work, the characterization of the scientific CCDs that will arrive to LSC soon. This CCDs is similar at the ones installed at the prototype LBC that have already give science results. The idea once is characterize would be to prove if this can be an assay infrastructure.

For the particle identification, being able to measure angles to defined direction and determine whether the incoming muons have a preferred direction, specifically towards the CMS interaction point. Additionally, the DNN could be used to investigate muon diffusion in CCDs.

Bibliography

- [1] Arbey, A. and Mahmoudi, F., *Dark matter and the early Universe: A review*, Progress in Particle and Nuclear Physics, vol. 119, pp. 103865, Jul. 2021. DOI: 10.1016/j.ppnp.2021.103865. Available: <http://dx.doi.org/10.1016/j.ppnp.2021.103865>.
- [2] Marrodan T., Rauch L. *Dark matter direct-detection experiments*, arXiv:1509.08767v2 [physics.ins-det], (2015). Available at: <https://doi.org/10.48550/arXiv.1509.08767>
- [3] Smith G. E. *The invention and early history of the CCD*, Nuclear Instruments and Methods in Physics Research Section A: Accelerators, Spectrometers, Detectors and Associated Equipment, vol. 607, no. 1, pp. 1-6, 2009. Radiation Imaging Detectors 2008. ISSN: 0168-9002. doi: <https://doi.org/10.1016/j.nima.2009.03.233>. URL:<https://www.sciencedirect.com/science/article/pii/S0168900209005877>.
- [4] M. F. Sofo, *Sensores Multipixel CCD de Ultra Bajo Ruido de Lectura para Detección de Partículas*. Ingeniería Eléctrica y Electrónica. Instituto Balseiro (2017). Available at: <https://ri.conicet.gov.ar/handle/11336/115059>
- [5] Claudia de Dominicis. *Search for light dark matter with DAMIC-M experiment*. Instrumentation and Detectors [physics.ins-det]. Ecole nationale supérieure Mines-Télécom Atlantique, (2022). English. NNT : 2022IMTA0313. tel-03884152
- [6] J. Tiffenberg, *Counting electrons with the Skipper-CCD*, slide presentation, Fermi National Laboratory, (2020). Available at: http://lambda.df.uba.ar/files/URA_skipper.pdf
- [7] Janesick J. R., et al. *New advancements in charge-coupled device technology: subelectron noise and 4096 x 4096 pixel CCDs*, International Society for Optics and Photonics, SPIE, doi:10.1117/12.19452, (1990). Available at: <https://doi.org/10.1117/12.19452>
- [8] DAMIC-M Collaboration, *The DAMIC-M Experiment: Status and First Results*, arXiv:2210.12070 [hep-ex], (2022). Available at: <https://arxiv.org/abs/2210.12070>
- [9] Lee, S.J., Kilminster, B., Macchiolo, A., *Dark Matter in CCDs at Modane (DAMIC-M): a silicon detector apparatus searching for low-energy physics processes*, Journal of Instrumentation, vol. 15, no. 02, pp. C02050–C02050, (2020). Available at: <http://dx.doi.org/10.1088/1748-0221/15/02/C02050>

- [10] Holland, S. E. *Physics of fully depleted CCDs*. Journal of Instrumentation, 9(03), C03057–C03057. IOP Publishing. arXiv:1403.6185 [astro-ph.IM], (2014). Available at: <http://dx.doi.org/10.1088/1748-0221/9/03/C03057>.
- [11] DAMIC-M Collaboration, *Precision measurement of Compton scattering in silicon with a skipper CCD for dark matter detection*, arXiv:2207.00809v1 [physics.ins-det], (2022). Available at: <https://arxiv.org/abs/2207.00809>
- [12] Detector - DAMIC-M. *DAMIC-M* [on-line]. Available at: <https://damicm.cnrs.fr/en/detector/>
- [13] Privitera, P. et al. *First Constraints from DAMIC-M on Sub-GeV Dark-Matter Particles Interacting with Electrons*. Physical Review Letters, American Physical Society (APS), (2023). DOI: [10.1103/physrevlett.130.171003](https://doi.org/10.1103/physrevlett.130.171003). Available at <https://arxiv.org/abs/2302.02372v1>
- [14] Estrada J. *Low Threshold Acquisition controller for Skipper CCDs*, arXiv:2004.07599v1 [astro-ph.IM] , (2020). Available at: <https://arxiv.org/pdf/2004.07599.pdf>
- [15] Pérez M. *Caracterización de aparatos de carga acoplada (CCDS) con sistema de lectura skipper*, (2023). Available at: <https://hdl.handle.net/10902/30223>
- [16] CERN. 2024. *The LHC: Machine Status Report*. Geneva: CERN. Available at: <https://edms.cern.ch/ui/file/2872429/2.0/2024-LHC-V2.0.pdf>.
- [17] Evans L. and Bryant P. *LHC Machine*. *JINST* **3** S08001. (2008). Published by IOP Publishing Ltd. DOI: [10.1088/1748-0221/3/08/S08001](https://doi.org/10.1088/1748-0221/3/08/S08001). Available at: <https://iopscience.iop.org/article/10.1088/1748-0221/3/08/S08001>.
- [18] Christopher S. Hill et al., *Search for millicharged particles in proton-proton collisions at $\sqrt{s} = 13$ TeV*, arXiv:2005.06518 [hep-ex], (2020). Available at: <https://doi.org/10.48550/arXiv.2005.06518>
- [19] Estrada J. et al., *SENSEI: First Direct-Detection Constraints on sub-GeV Dark Matter from a Surface Run*, arXiv:1804.00088 [hep-ex], (2018). Published in: *Phys. Rev. Lett.* **121**, 061803 (2018). Available at: <https://doi.org/10.48550/arXiv.1804.00088>
- [20] Perez S. E., et al. *SENSEI: Search for Millicharged Particles produced in the NuMI Beam*. arXiv:2305.04964v2 [hep-ex]. Available at: <https://arxiv.org/pdf/2305.04964v2.pdf>
- [21] T. Emken et al., *Direct detection of strongly interacting sub-GeV dark matter via electron recoils*, *JCAP* **09**, 070 (2019), DOI: [10.1088/1475-7516/2019/09/070](https://doi.org/10.1088/1475-7516/2019/09/070).
- [22] R. Foot, A. Kobakhidze, *A simple explanation of the PVLAS anomaly in spontaneously broken mirror models*, *Physics Letters B*, Volume 650, Issue 1, 2007, Pages 46-48, ISSN 0370-2693, DOI: [10.1016/j.physletb.2007.04.045](https://doi.org/10.1016/j.physletb.2007.04.045). Available at: <https://www.sciencedirect.com/science/article/pii/S0370269307005199>.
- [23] H. Gies, J. Jaeckel, A. Ringwald, *Accelerator Cavities as a Probe of Millicharged Particles*, *Europhys. Lett.* **76**, 794-800 (2006), DOI: [10.1209/epj/i2006-10356-5](https://doi.org/10.1209/epl/i2006-10356-5). Available at: <https://doi.org/10.48550/arXiv.hep-ph/0608238>.

- [24] Q. Wallemacq, J.-R. Cudell, *Dark antiatoms can explain DAMA*, *JCAP* **02**, 011 (2015), DOI: [10.1088/1475-7516/2015/02/011](https://doi.org/10.1088/1475-7516/2015/02/011). Available at: <https://doi.org/10.1088/1475-7516/2015/02/011>.
- [25] A. N. Khan, *Can nonstandard neutrino interactions explain the XENON1T spectral excess?*, *Physics Letters B*, Volume 809, 135782 (2020), ISSN 0370-2693, DOI: [10.1016/j.physletb.2020.135782](https://doi.org/10.1016/j.physletb.2020.135782). Available at: <https://www.sciencedirect.com/science/article/pii/S0370269320305852>.
- [26] Y. Farzan, M. Rajaee, *Pico-charged particles explaining 511 keV line and XENON1T signal*, arXiv:2007.14421 [hep-ph] (2020). Available at: <https://arxiv.org/abs/2007.14421>.
- [27] R. Plestid et al., *Constraints on millicharged particles from cosmic-ray production*, *Phys. Rev. D* **102**, 115032 (2020), DOI: [10.1103/physrevd.102.115032](https://doi.org/10.1103/physrevd.102.115032). Available at: [http://dx.doi.org/10.1103/PhysRevD.102.115032](https://dx.doi.org/10.1103/PhysRevD.102.115032).
- [28] Kumar, P., et al., *A comprehensive review on dark current in perovskite photodetectors: Origin, drawbacks, and reducing strategies*. Sensors and Actuators A: Physical, vol. 369, 2024, pp. 115076. DOI: <https://doi.org/10.1016/j.sna.2024.115076>. Available: <https://www.sciencedirect.com/science/article/pii/S0924424724000694>.
- [29] Janesick, J.R. *Scientific Charge-Coupled Devices*. PM83. 2001. 924 pages. ISBN: 9780819436986. Available at: <https://api.semanticscholar.org/CorpusID:119869286>.
- [30] Castello, N. *Documentation for pysimdamicm package - waders 5.3.1 documentation*. Available at: <https://ncastell.web.cern.ch/ncastell/pysimdamicm/index.html>
- [31] Chavarria, A., et al., *Measurement of radioactive contamination in the high-resistivity silicon CCDs of the DAMIC experiment*. Journal of Instrumentation, 10(08), P08014–P08014. (2015) arXiv:1506.02562v2 Available at: [http://dx.doi.org/10.1088/1748-0221/10/08/P08014](https://doi.org/10.1088/1748-0221/10/08/P08014).

Appendix A: Abbreviations

ADUs Analog-to-Digital Units

ALMA Atacama Large Millimeter Array

CCDs Charge Coupled Devices

CDS Correlated Double Sampling

CMS Compact Muon Solenoid

DAMIC-M DArk Matter In CCDs at Modane

DES Dark Energy Survey

DESI Dark Energy Spectroscopic Instrument

DD Direct Detection

DG Dump Gate

DM Dark Matter

DNN Deep Neural Network

Fermilab Fermi National Accelerator Laboratory

IFCA Instituto de Física de Cantabria

ID Indirect Detection

LBC Low Background Chamber

LHC Large Hadron Collider

LTA Low Threshold Acquisition

LSC Laboratorio Subterráneo de Canfranc

LSM Laboratoire Souterrain de Modane

MOS Metal-Oxide-Semiconductor

MOSKITA MOBILE SKIpper Testing Apparatus

mCPs milliCharged Particles

PNNL Pacific Northwest National Laboratory

SC Slow Control

SENSEI Sub-Electron-Noise Skipper CCD Experimental Instrument

SM Standard Model

SN Sense Node

SNOLAB Sudbury Neutrino Observatory Laboratory

SW Summing Well

TG Transfer Gate

WIMPs Weakly Interacting Massive Particles

YOLO You Only Look Once

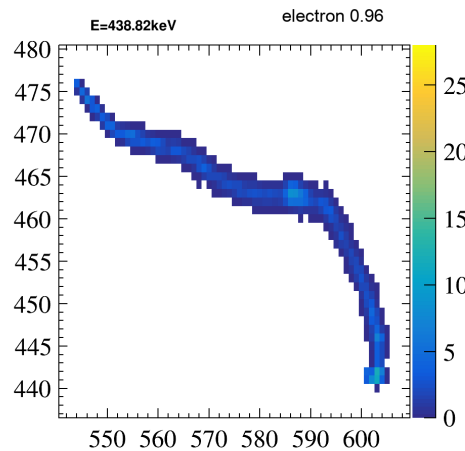
Appendix B: Code Repository

The codes used in this thesis are available in the following GitHub repository: <https://github.com/Perezzi11/TFM> Within the `/scripts/` folder of the repository, the following files can be found:

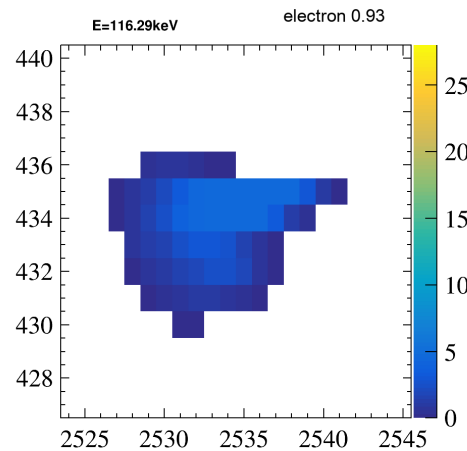
- `clean_expose_binned.xml`: This file is the sequencer and from where we can change the clock delays and where to send the charge.
- `run_variables.sh`: In this file, we can change the number of skips, the CDS integration times, the exposition time, the bias voltage and the dimensions of the CCD that are going to be read.
- `voltage_setup.xml`: In this script we can change the values for the voltages of the clocks and of the gates
- `panaSKIImg_config_LTA_proc.json`: This file contains the different WADERS processes to clean the data.
- `hot_columns_2.py`: In this script, it is included the calculation of both the dark current and the gain, as well as the implementation of the hot column detection algorithm.
- `Optimization_hot_columns.py`: In this script, we obtain the optimal value for the sigma to optimize the hot column detection.
- `NN_muons.py`: This script is used for the training and prediction of the DNN.
- `results_file.py`: This file should be replaced with `results.py` from the Ultralytics package for better visualization of the detected clusters.

Appendix C: DNN Prediction Images

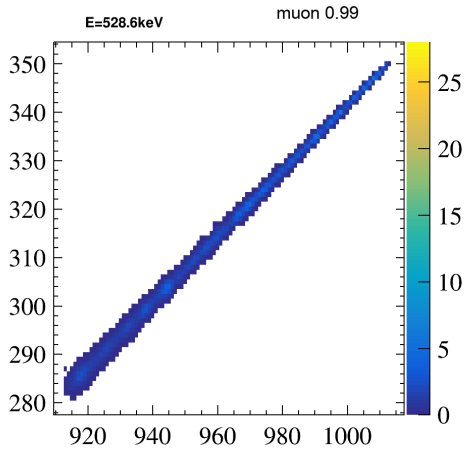
In this appendix we are going to show different predictions from the DNN. The confidence of the prediction is at the top right corner of the image.



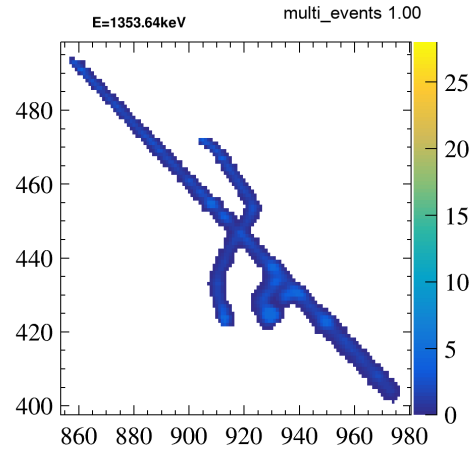
Electron predicted.



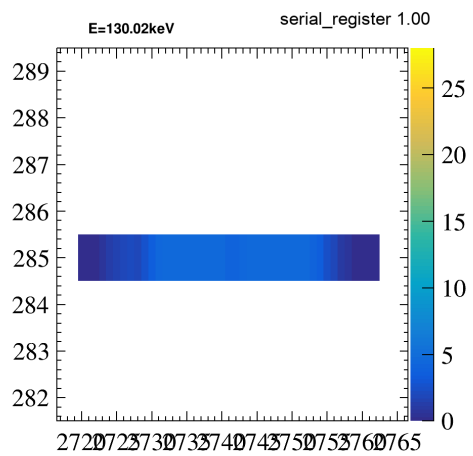
Electron predicted.



Muon predicted.



Multiple events predicted.



Serial register event predicted